
This copy is for your personal, non-commercial use only.

If you wish to distribute this article to others, you can order high-quality copies for your colleagues, clients, or customers by [clicking here](#).

Permission to republish or repurpose articles or portions of articles can be obtained by following the guidelines [here](#).

The following resources related to this article are available online at www.sciencemag.org (this information is current as of August 11, 2011):

Updated information and services, including high-resolution figures, can be found in the online version of this article at:

<http://www.sciencemag.org/content/333/6044/838.full.html>

Supporting Online Material can be found at:

<http://www.sciencemag.org/content/suppl/2011/08/10/333.6044.838.DC1.html>

<http://www.sciencemag.org/content/suppl/2011/08/10/333.6044.838.DC2.html>

This article **cites 31 articles**, 5 of which can be accessed free:

<http://www.sciencemag.org/content/333/6044/838.full.html#ref-list-1>

This article has been **cited by** 1 articles hosted by HighWire Press; see:

<http://www.sciencemag.org/content/333/6044/838.full.html#related-urls>

This article appears in the following **subject collections**:

Materials Science

http://www.sciencemag.org/cgi/collection/mat_sci

Epidermal Electronics

Dae-Hyeong Kim,^{1*} Nanshu Lu,^{1*} Rui Ma,^{2*} Yun-Soung Kim,¹ Rak-Hwan Kim,¹ Shuodao Wang,³ Jian Wu,³ Sang Min Won,¹ Hu Tao,⁴ Ahmad Islam,¹ Ki Jun Yu,¹ Tae-il Kim,¹ Raeed Chowdhury,² Ming Ying,¹ Lizhi Xu,¹ Ming Li,^{3,6} Hyun-Joong Chung,¹ Hohyun Keum,¹ Martin McCormick,² Ping Liu,⁵ Yong-Wei Zhang,⁵ Fiorenzo G. Omenetto,⁴ Yonggang Huang,³ Todd Coleman,² John A. Rogers^{1†}

We report classes of electronic systems that achieve thicknesses, effective elastic moduli, bending stiffnesses, and areal mass densities matched to the epidermis. Unlike traditional wafer-based technologies, laminating such devices onto the skin leads to conformal contact and adequate adhesion based on van der Waals interactions alone, in a manner that is mechanically invisible to the user. We describe systems incorporating electrophysiological, temperature, and strain sensors, as well as transistors, light-emitting diodes, photodetectors, radio frequency inductors, capacitors, oscillators, and rectifying diodes. Solar cells and wireless coils provide options for power supply. We used this type of technology to measure electrical activity produced by the heart, brain, and skeletal muscles and show that the resulting data contain sufficient information for an unusual type of computer game controller.

Physiological measurement and stimulation techniques that exploit interfaces to the skin have been of interest for more than 80 years, beginning in 1929 with electroencephalography from the scalp (1–3). Nearly all associated device technologies continue, however, to rely on conceptually old designs. Typically, small numbers of bulk electrodes are mounted on the skin via adhesive tapes, mechanical clamps or straps, or penetrating needles, often mediated by conductive gels, with terminal connections to separate boxes that house collections of rigid circuit boards, power supplies, and communication components (4–9). These systems have many important capabilities, but they are poorly suited for practical application outside of research labs or clinical settings because of difficulties in establishing long-lived, robust electrical contacts that do not irritate the skin and in achieving integrated systems with overall sizes, weights, and shapes that do not cause discomfort during prolonged use (8, 9). We introduce a different approach, in which the electrodes, electronics, sensors, power supply, and communication components are configured together into ultrathin, low-modulus, lightweight, stretchable

“skin-like” membranes that conformally laminate onto the surface of the skin by soft contact, in a manner that is mechanically invisible to the user, much like a temporary transfer tattoo.

Materials, mechanics, and design strategies.

A demonstrative platform is shown in Fig. 1, integrating a collection of multifunctional sensors (such as temperature, strain, and electrophysiological), microscale light-emitting diodes (LEDs), active/passive circuit elements (such as transistors, diodes, and resistors), wireless power coils, and devices for radio frequency (RF) communications (such as high-frequency inductors, capacitors, oscillators, and antennae), all integrated on the surface of a thin (~30 μm), gas-permeable elastomeric sheet based on a modified polyester (BASF, Ludwigshafen, Germany) with low Young's modulus (~60 kPa) (fig. S1A). The devices and interconnects exploit ultrathin layouts (<7 μm), neutral mechanical plane configurations, and optimized geometrical designs. The active elements use established electronic materials, such as silicon and gallium arsenide, in the form of filamentary serpentine nanoribbons and micro- and nanomembranes. The result is a high-performance system that offers reversible, elastic responses to large strain deformations with effective moduli (<150 kPa), bending stiffnesses (<1 nN m), and areal mass densities (<3.8 mg/cm²) that are orders of magnitude smaller than those possible with conventional electronics or even with recently explored flexible/stretchable device technologies (10–19). Water-soluble polymer sheets [polyvinyl alcohol (PVA) (Aicello, Toyohashi, Japan); Young's modulus, ~1.9 GPa; thickness, ~50 μm (fig. S1B)] serve as temporary supports for manual mounting of these systems on the skin in an overall construct that is directly analogous to that of a temporary transfer tattoo. The image in Fig. 1B, top, is of a device similar to the one in Fig. 1A, after mounting it onto the skin by washing away the PVA and then partially

peeling the device back with a pair of tweezers. When completely removed, the system collapses on itself because of its extreme deformability and skin-like physical properties, as shown in Fig. 1B, bottom (movie S1). The schematic illustration in the inset shows an approximate cross-sectional layout.

These mechanical characteristics lead to robust adhesion to the skin via van der Waals forces alone, without any mechanical fixturing hardware or adhesive tapes. The devices impose negligible mechanical or mass loading (typical total mass of ~0.09 g), as is evident from the images of Fig. 1C, which show the skin deforming freely and reversibly, without any apparent constraints in motion due to the devices. Electronics in this form can even be integrated directly with commercial temporary transfer tattoos as a substrate alternative to polyester or PVA. The result, shown in Fig. 1D, is of possible interest as a way to conceal the active components and to exploit low-cost materials (the substrate, adhesives, and backing layers) already developed for temporary transfer tattoos (movie S1). Potential uses include physiological status monitoring, wound measurement/treatment, biological/chemical sensing, human-machine interfaces, covert communications, and others.

Understanding the mechanics of this kind of device, the mechanophysiology of the skin, and the behavior of the coupled abiotic-biotic system are all important. For present purposes, the skin can be approximated as a bilayer, consisting of the epidermis (modulus, 140 to 600 kPa; thickness, 0.05 to 1.5 mm) and the dermis (modulus, 2 to 80 kPa; thickness, 0.3 to 3 mm) (20–23). This bilayer exhibits linear elastic response to tensile strains $\leq 15\%$, which transitions to nonlinear behavior at higher strains, with adverse, irreversible effects beyond 30% (24). The surface of the skin has wrinkles, creases, and pits with amplitudes and feature sizes of 15 to 100 μm (25) and 40 to 1000 μm (26), respectively. The devices described here (Fig. 1) have moduli, thicknesses, and other physical properties that are well matched to the epidermis, with the ability to conform to the relief of its surface. We therefore refer to this class of technology as an “epidermal electronic system” (EES).

Macroscopically, an EES on skin can be treated as a thin film on an epidermis–dermis bilayer substrate. Microscopically, the sizes of the individual electronic components and interconnects are comparable with those of relief features on the skin and therefore must be considered explicitly. We began by considering aspects of adhesion, in the macroscopic limit. Globally, detachment can occur in either tension or compression because of interfacial cracks that initiate at the edges or the central regions of the EES, respectively. Low effective moduli and small thicknesses minimize the deformation-induced stored elastic energy that drives both of these failure modes. Analytical calculation (27) shows that

¹Department of Materials Science and Engineering, Beckman Institute for Advanced Science and Technology, and Frederick Seitz Materials Research Laboratory, University of Illinois at Urbana-Champaign, Urbana, IL 61801, USA. ²Department of Electrical and Computer Engineering, Coordinated Science Laboratory, University of Illinois at Urbana-Champaign, Urbana, IL 61801, USA. ³Department of Mechanical Engineering and Department of Civil and Environmental Engineering, Northwestern University, Evanston, IL 60208, USA. ⁴Department of Biomedical Engineering, Tufts University, Medford, MA 02155, USA. ⁵Institute of High Performance Computing, 1 Fusionopolis Way, #16-16 Connexis, 138632, Singapore. ⁶State Key Laboratory of Structural Analysis for Industrial Equipment, Dalian University of Technology, Dalian 116024, China.

*These authors contributed equally to this work.

†To whom correspondence should be addressed. E-mail: jrogers@uiuc.edu

compared with silicon chips (thickness of ~ 1 mm) and sheets of polyimide (thickness of ~ 75 μm), the driving forces for delamination of the EES/skin interface are reduced by more than seven and four orders of magnitude, respectively. Measurements and theoretical calculations (27) shown in Fig. 2A explore the relevant scaling behaviors in structures that provide simplified, macroscopic models of EES/skin. The experiments use sheets of polyester (~ 2 mm thick) for the skin and films of poly(dimethylsiloxane) (PDMS) (Dow Corning, Midland, USA) for the EES. The critical delamination strain is plotted in Fig. 2A as a function of PDMS thickness for two different formulations: one with a modulus of 19 kPa (50:1) and

the other 145 kPa (30:1) (fig. S1C). The results, both theory and experiment, confirm that reducing the modulus and thickness lowers the driving forces for interface delamination for a given applied strain (bending or stretching) without lower bound.

The mechanical properties of the EES depend on the effective modulus and thickness of both the circuits and sensors and the substrate. In samples such as those in Fig. 1, the properties of the active components and interconnects can dominate the mechanics of the overall system. The in-plane layouts and materials of this layer are therefore key design parameters. Recent work in stretchable electronics establishes that the

overall range of deformability can be optimized in systems composed of active devices joined together in open-mesh structures by non-coplanar interconnects in neutral mechanical plane configurations, in which elastomers with relatively large moduli (2 to 10 MPa) and thicknesses (millimeters to centimeters) serve as substrates (13, 14). For EES, the effective modulus (E_{EES}) and bending stiffness ($E_{\text{EES}}I$), rather than the range of stretchability, are paramount. These requirements demand alternative designs and choices of materials. If we assume that the effective moduli of the individual devices (for example, Young's modulus ~ 160 GPa for Si and ~ 90 GPa for GaAs) are much higher than those of the

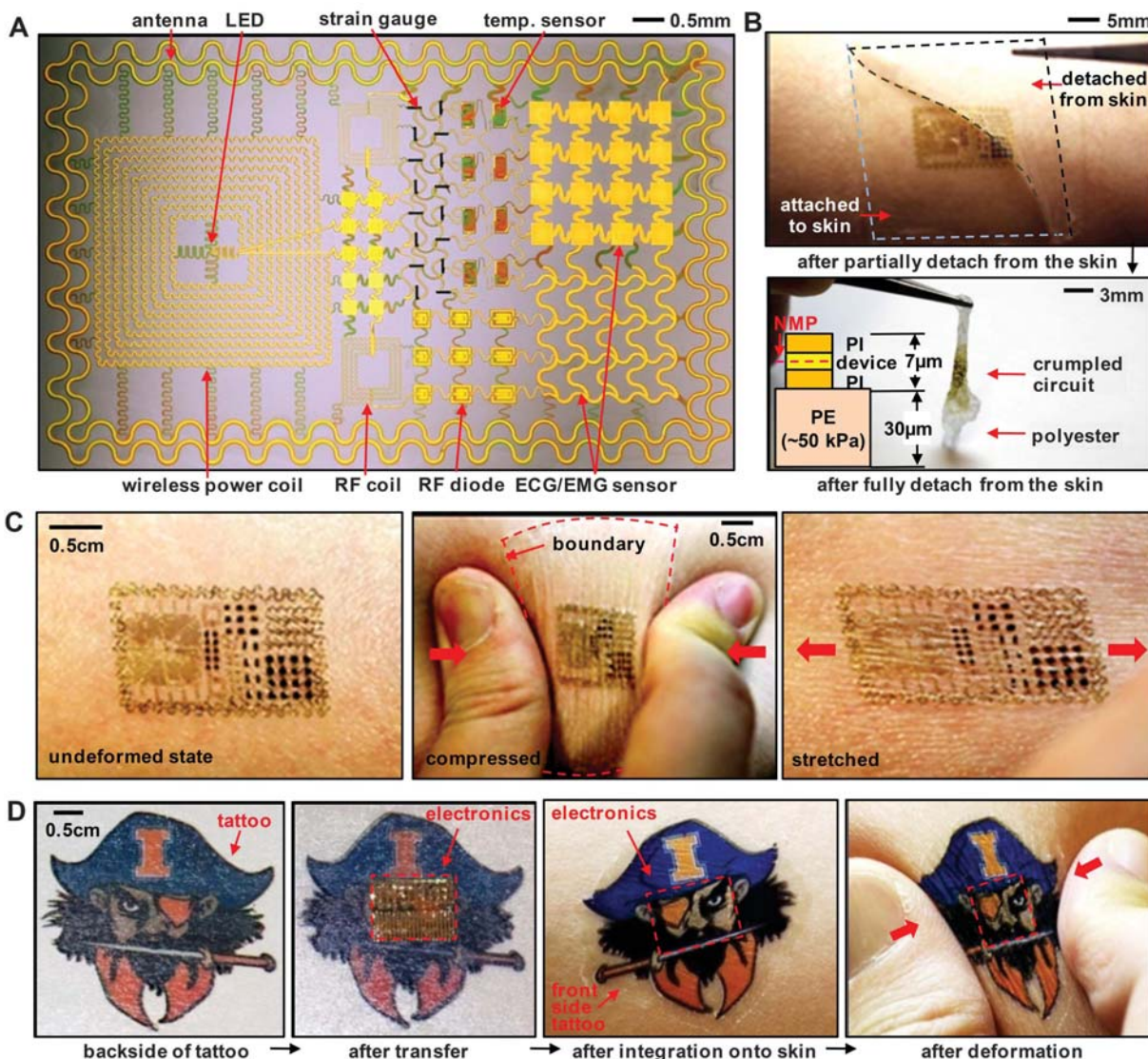


Fig. 1. (A) Image of a demonstration platform for multifunctional electronics with physical properties matched to the epidermis. Mounting this device on a sacrificial, water-soluble film of PVA, placing the entire structure against the skin, with electronics facing down, and then dissolving the PVA leaves the device conformally attached to the skin through van der Waals forces alone, in a format that imposes negligible mass or mechanical loading effects on the skin. (B) EES partially (top) and fully (bottom) peeled away from the skin. (Inset) A representative cross-sectional illustration of the struc-

ture, with the neutral mechanical plane (NMP) defined by a red dashed line. (C) Multifunctional EES on skin: undeformed (left), compressed (middle), and stretched (right). (D) A commercial temporary transfer tattoo provides an alternative to polyester/PVA for the substrate; in this case, the system includes an adhesive to improve bonding to the skin. Images are of the backside of a tattoo (far left), electronics integrated onto this surface (middle left), and attached to skin with electronics facing down in undeformed (middle right) and compressed (far right) states.

interconnects and that the interconnected device components (rather than the substrate) dominate the mechanics, then we can write the approximate expression $E_{EES} = E_{int}(1 + L_d/L_s)$, where E_{int} is the effective modulus of the interconnects, L_d is the characteristic device size, and L_s is the distance between devices, as illustrated in fig. S1D. The value of E_{EES} can be minimized by reducing E_{int} and L_d/L_s . For the former, thin narrow interconnect lines formed into large-amplitude “filamentary serpentine” (FS) shapes represent effective designs. For the latter, ultrathin active devices that adopt similar FS layouts and continuously integrate with FS interconnects reduce the effective value of L_d to zero. The value of E_{EES} decreases rapidly with the thicknesses of the devices, interconnects, and substrate. An ultrathin FS construct is shown in Fig. 2B, left, with a cross-sectional schematic illustration as an inset. Results of tensile testing

(Fig. 2B, right) indicate that such FS-EES samples (Fig. 2B, left) achieve E_{EES} (~140 kPa) and EI_{EES} (~0.3 nNm) (27) that are comparable with the epidermis and more than one and five orders of magnitude smaller than previously reported stretchable electronic devices, respectively (28). Furthermore, highly repeatable loading and unloading stress-strain curves up to strains of 30% demonstrate purely elastic responses, with maximum principal strains in the metals that are less than ~0.2% (fig. S1E). Calculations yield effective tensile moduli (Fig. 2B, right), with excellent correspondence to experiment. Such FS layouts can maintain nearly 20% areal contact of active elements with the skin, for effective electrical interfaces. In certain applications, layouts that involve some combination of FS geometries and device islands (L_d not equal to zero) connected by FS interconnects (Fig. 1 and fig. S1F) can be used, with expected consequences on the local

mechanics (fig. S1G). In both options, suitable designs lead to mechanical and adhesive properties that allow conformal adhesion to the skin and minimal loading effects (Fig. 2C). Without optimized layouts, we observed delamination under similar conditions of deformation (fig. S1H), which is consistent with the fracture modes illustrated in Fig. 2A.

For many uses of EES, physical coupling of devices to the surface of the skin is important. Confocal micrographs of EES mounted on pig skin appear in Fig. 2, D and E, as well as fig. S2C [dye information and bare pig skin confocal micrographs are shown in fig. S2, A and B, respectively; sample preparation and imaging procedures can be found in (27)]. With FS structures, the results show remarkably conformal contact, not only at the polyester regions of the EES but also at the FS elements (Fig. 2, D and E). Similar behavior was obtained, but in a less ideal

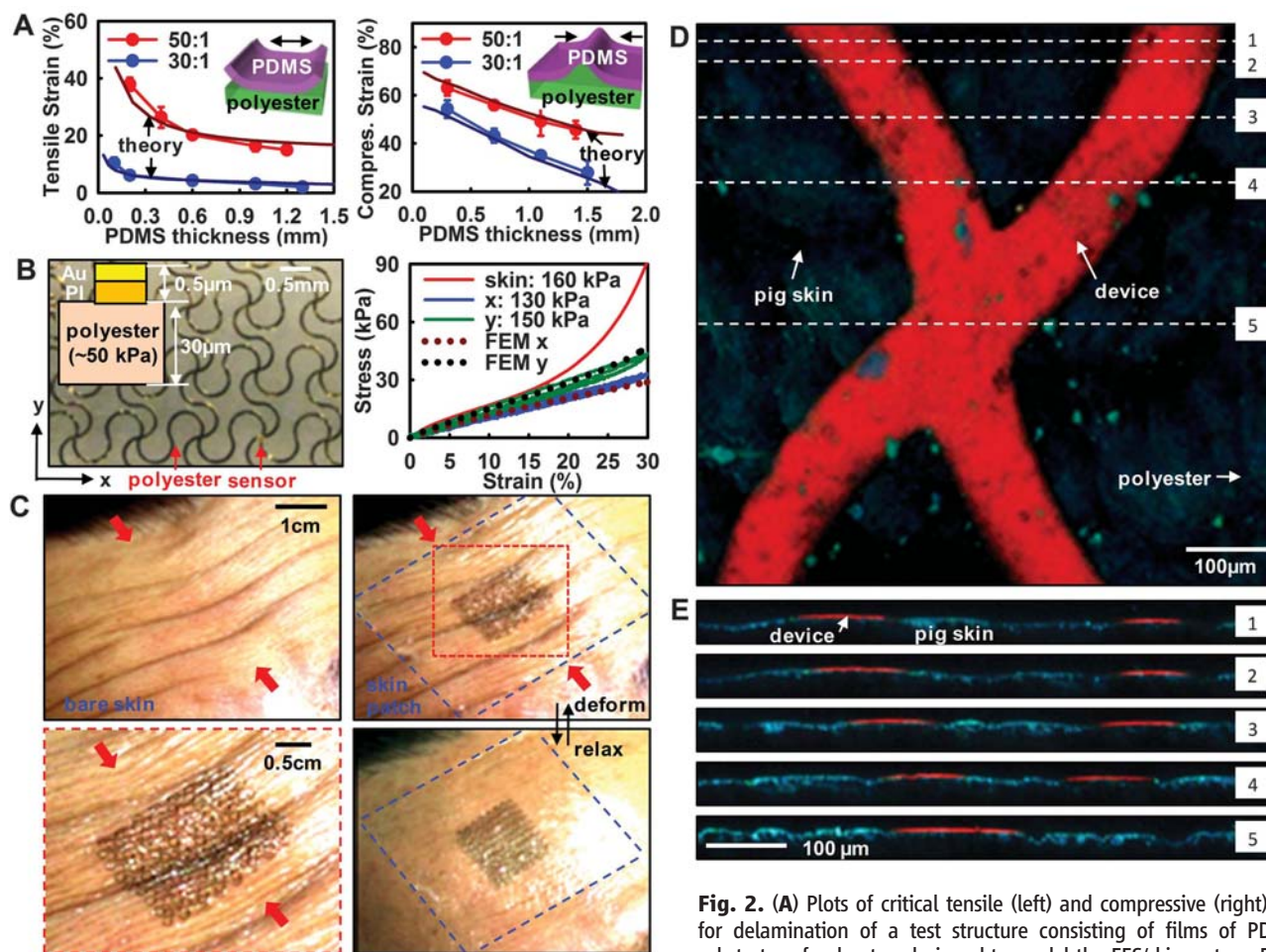


Fig. 2. (A) Plots of critical tensile (left) and compressive (right) strains for delamination of a test structure consisting of films of PDMS on substrates of polyester, designed to model the EES/skin system. Data for formulations of PDMS with two different moduli are shown (red, 19 kPa; blue, 145 kPa). The critical strains increase as the PDMS thickness and modulus decrease, which is consistent with modeling results (lines). (B) Optical micrograph of an EES with FS design (left). The plot (right) shows the stress-strain data from uniaxial tensile measurements for two orthogonal directions. Data collected from a sample of pig skin are also presented. The dotted lines correspond to calculations performed with finite element modeling. (C) Skin of the forehead before (top left) and after the mounting of a representative FS-EES, at various magnifications and states of deformation. The dashed blue boxes at right highlight the outer boundary of the device. The red arrows indicate the direction of compressive strains generated by a contraction of facial muscles. The red dashed box at the top right corresponds to the field of view of the image in the bottom left. (D) Confocal microscope image (top view) at the vicinity of the contacting interface between an FS-EES laminated on a sample of pig skin. The FS structure and the skin are dyed with red and blue fluorophores, respectively. (E) Cross-sectional confocal images at locations corresponding to the numbered, white dashed lines shown in the top-view frame above.

blue, 145 kPa). The critical strains increase as the PDMS thickness and modulus decrease, which is consistent with modeling results (lines). (B) Optical micrograph of an EES with FS design (left). The plot (right) shows the stress-strain data from uniaxial tensile measurements for two orthogonal directions. Data collected from a sample of pig skin are also presented. The dotted lines correspond to calculations performed with finite element modeling. (C) Skin of the forehead before (top left) and after the mounting of a representative FS-EES, at various magnifications and states of deformation. The dashed blue boxes at right highlight the outer boundary of the device. The red arrows indicate the direction of compressive strains generated by a contraction of facial muscles. The red dashed box at the top right corresponds to the field of view of the image in the bottom left. (D) Confocal microscope image (top view) at the vicinity of the contacting interface between an FS-EES laminated on a sample of pig skin. The FS structure and the skin are dyed with red and blue fluorophores, respectively. (E) Cross-sectional confocal images at locations corresponding to the numbered, white dashed lines shown in the top-view frame above.

fashion (fig. S2C), with layouts that incorporate device islands. These observations are consistent with analytical mechanics treatments that use macroscopic models of the EES and account for microscopic structures on the skin (27). Related calculations suggest that spontaneous pressures created by surface interactions are ~ 10 kPa (fig. S10B), which is below the sensitivity of human skin (~ 20 kPa) (29) but still sufficient to offer reasonable adhesion. Microscopic models indicate that these interactions generate compressive forces (per unit length) of ~ 0.1 N/m for each FS strip (27). Improved bonding can be achieved by using adhesives that are built into platforms for temporary transfer tattoos, as in Fig. 1D.

Multifunctional operation. A key capability of EES is in monitoring electrophysiological (EP) processes related to activity of the brain [electroencephalograms (EEGs)], the heart [electrocardiograms (ECGs)] and muscle tissue [electromyograms (EMGs)]. Amplified sensor electrodes that incorporate silicon metal oxide semiconductor field effect transistors (MOSFETs) in circuits in which all components adopt FS designs provide devices for this purpose. Here, the gate of a FS-MOSFET connects to an extended FS electrode for efficient coupling to the body potential (Fig.

3A; the inset shows an analogous design based on a rectangular device island and FS interconnects) via contact with the skin in a common-source amplifier configuration (Fig. 3B, left). The measured frequency response at different input capacitances (C_{IN}) is indicated in Fig. 3B, right, and is in quantitative agreement with circuit simulations (fig. S3, A and B). The value of C_{IN} is determined by a series combination of capacitances of the gate electrode, the encapsulating PI, and junction between the gate electrode and the body surface. The bandwidth matches requirements for high-performance EP recording. A typical layout for this purpose includes four amplified channels, each comprising a FS-MOSFET, a silicon-based FS resistor, and an FS electrode. One channel provides a reference, whereas the others serve as sites for measurement. Results of demonstration experiments appear subsequently.

Many other classes of semiconductor devices and sensors are also possible in EES, including resistance-based temperature sensors built with meander electrodes of Pt (Fig. 3C, left, and fig. S3C), in-plane strain gauges based on carbon-black-doped silicones (Fig. 3C, right, and fig. S3D), LEDs and photodetectors based on AlInGaP (for possible use in optical characteri-

zation of the skin/biofluids) (Fig. 3D, left, and fig. S3, E to G), and silicon FS photovoltaic cells (Fig. 3D, right). Such cells can generate a few tens of microwatts (fig. S3H); increasing the areas or areal coverages can improve the output, but not without compromises in size and mechanics. Wireless powering via inductive effects represents an appealing alternative. An example of an FS inductive coil connected to a microscale InGaN LED is shown in Fig. 3E, with electromagnetic modeling of its RF response. The resonance frequency (~ 35 MHz) matches that of a separately located transmission coil powered by an external supply. Voltage and current outputs in the receiver are sufficient to operate the microscale LEDs remotely, as shown in Fig. 3E. Such coils provide power directly in this example; they can also conceivably be configured to charge future classes of EES-integrated storage capacitors or batteries.

Examples of various RF components of the type needed for wireless communications or for scavenging RF energy are presented in Fig. 3, F and G. Shown in Fig. 3F is an optical image of silicon PIN diode (left) and its small-signal scattering parameters (fig. S3K), indicating insertion loss (S21 in forward condition) of < 6 dB and isolation (S21 in reverse condition) of > 15 dB

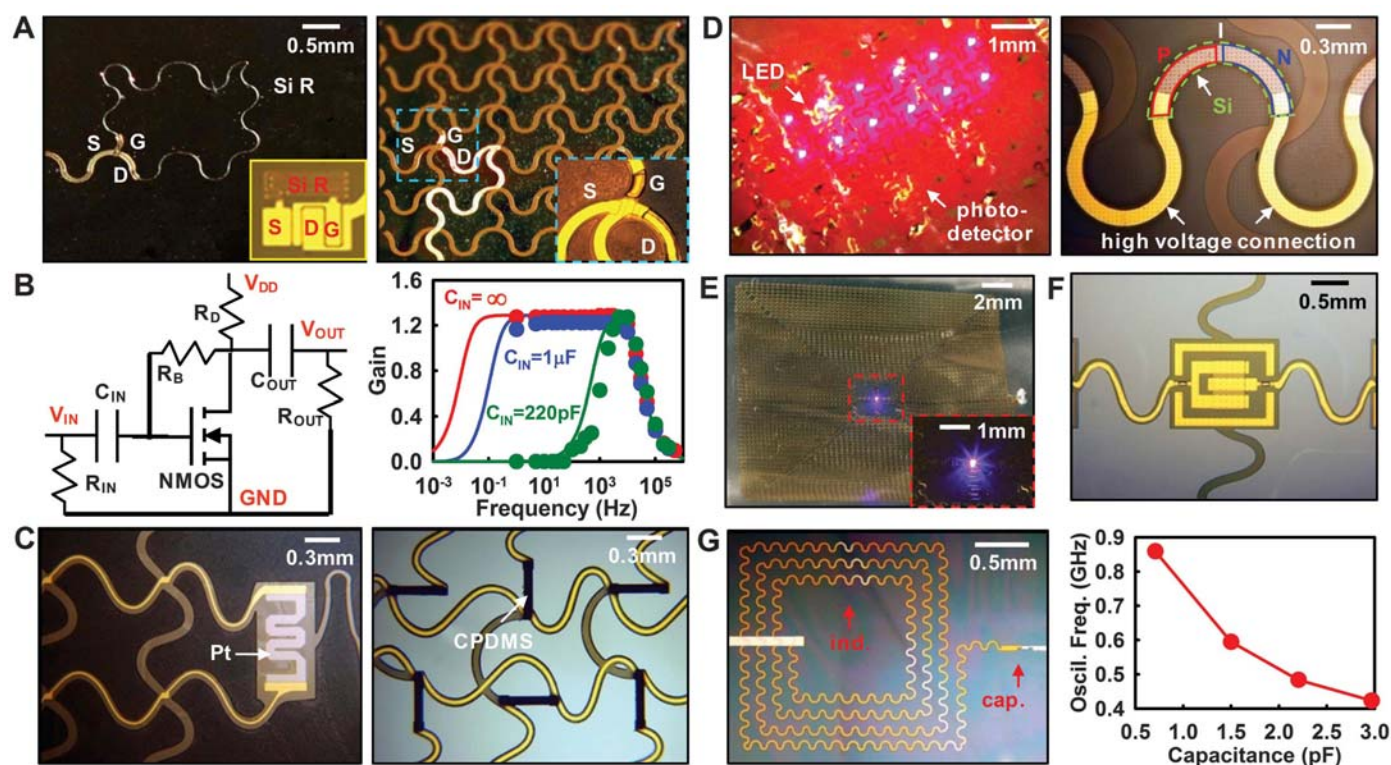


Fig. 3. (A) Optical micrographs of an active electrophysiological (EP) sensor with local amplification, as part of an FS-EES. (Left) The source, drain, and gate of a silicon MOSFET and a silicon feedback resistor before connection to sensor electrodes, all in FS layouts. (Inset) Similar device with island design. (Right) The final device, after metallization for the interconnects and sensor electrodes, with magnified view (inset). (B) Circuit diagram for the amplified EP sensor shown above (left). (Right) Measured and simulated frequency response for different input capacitance ($C_{IN} = \infty, 1\mu\text{F}, 220\text{pF}$). (C) Optical micrograph of a temperature sensor that uses a platinum resistor with FS interconnects (left)

and a strain gauge that uses electrically conductive silicone (CPDMS; right). (D) Image of an array of microscale AlInGaP LEDs and photodetectors, in an interconnected array integrated on skin, under compressive deformation (left) and of a FS silicon solar cell (right). (E) Image of a FS wireless coil connected to a microscale InGaN LED, powered by inductive coupling to a separate transmission coil (not in the field of view). (F) Optical micrograph of a silicon RF diode. (G) Optical micrograph of an interconnected pair of FS inductors and capacitors designed for RF operation (left). The graph at right shows resonant frequencies for LC oscillators built with different FS capacitors.

for frequencies of up to 2 GHz. Examples of FS inductors and capacitors and their RF responses appear in Fig. 3G and fig. S3L. Connecting pairs of such devices yields oscillators with expected resonant frequencies (Fig. 3G, right). A notable behavior is that the response varies with the state of deformation because of the dependence of the RF inductance on geometry. For example, at tensile strains of $\sim 12\%$ the resonance frequency shifts by $\sim 30\%$ (fig. S3, I and J). Such effects, which also appear in the wireless power coils but not in the other devices of Fig. 3, will influence the behavior of antenna structures and certain related RF components. These issues must be considered explicitly in EES design and modes of operation.

Systems for electrophysiological recording. EES configured for measuring ECG, EMG, and EEG in conformal, skin-mounted modes without conductive gels or penetrating needles provide important, system-level demonstrations (fig. S4A and movie S2) (27). All materials that come into direct contact with the skin (Au, PI, and polyester) are biocompatible (30, 31). Measurements involved continuous use for as many as 6 hours. Devices worn for up to 24 hours or more on the arm, neck, forehead, cheek, and chin showed no degradation or irritation to the skin (figs. S14 and S15). Devices mounted in challenging areas such as the elbow fractured and/or debonded under full-range motion (fig. S16). ECG recordings from the chest (27) revealed

high-quality signals with information on all phases of the heartbeat, including rapid depolarization of the cardiac wave, and the associated QRS complex (Fig. 4A, right) (32). EMG measured on the leg (27) with muscle contractions to simulate walking and resting are presented in Fig. 4B, left. The measurements agree remarkably well with signals simultaneously collected using commercial, bulk tin electrodes that require conductive gels, mounted with tapes at the same location (Fig. 4B, right, and fig. S4B, right). An alternative way to view the data (spectrogram) is shown in Fig. 4C, in which the spectral content appears in a color contour plot with frequency and time along the y and x axes, respectively. Each muscle contraction corresponds

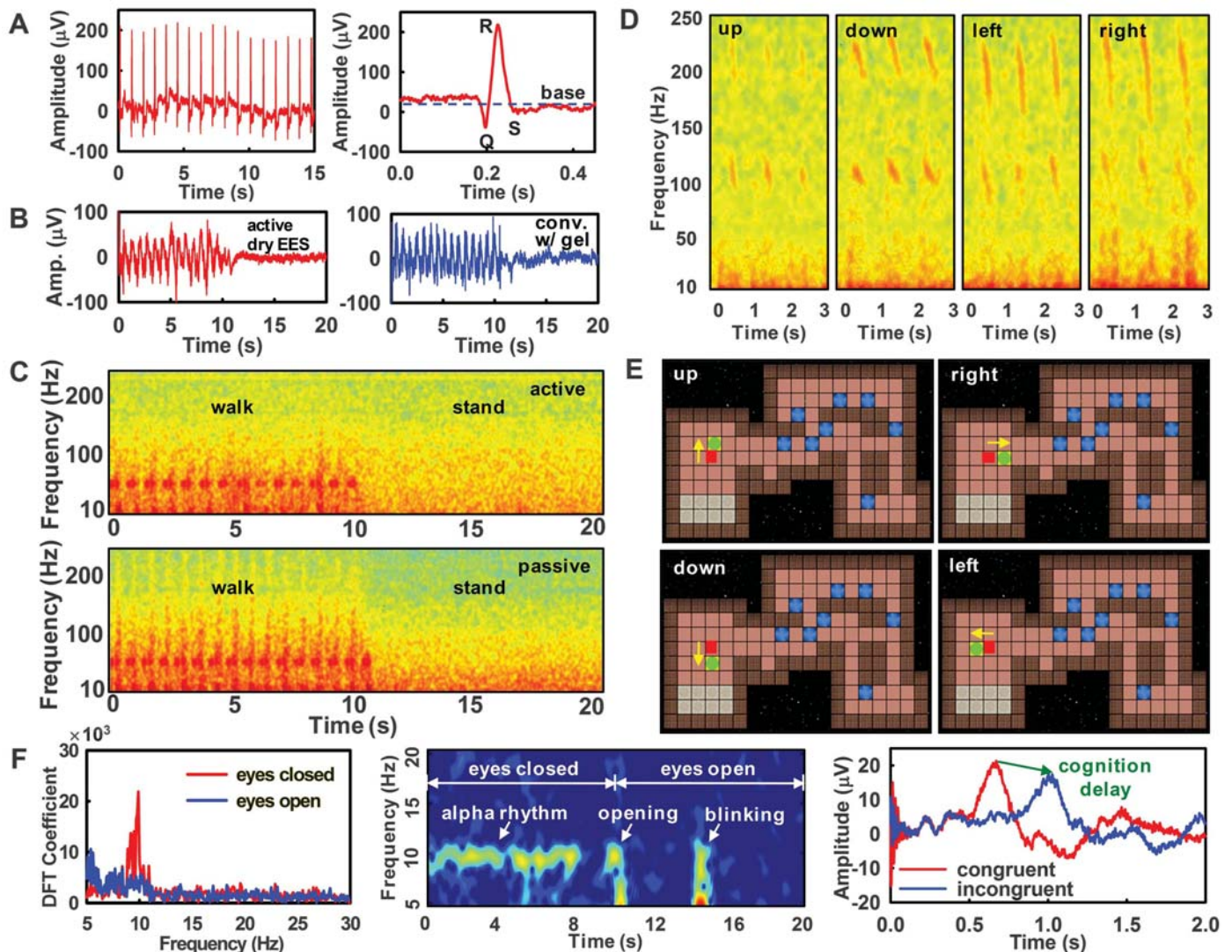


Fig. 4. (A) ECG signals measured with an active EES attached to the chest (left), and magnified view of data corresponding to a single heartbeat (right). (B) (Left) EMG measurements using an active EES, mounted on the right leg during simulated walking (from 0 to 10 s) and standing (from 10 to 20 s). (Right) Recordings collected with conventional sensors and conductive gel. (C) Spectrogram of the data in (B) for corresponding electrode type. (D) EMG spectrograms measured using an active EES mounted on the neck during vocalization of four different words: “up,” “down,” “left,” and “right.” (E)

Simulated video game control by pattern recognition on EMG data from (D). The player icon is moved from an initial position (red) to destination (green). (F) (Left) Discrete Fourier transform (DFT) coefficients of EEG alpha rhythms at ~ 10 Hz (27), measured with a passive EES. (Center) The spectrogram of the alpha rhythm. The first and next 10 s correspond to periods when the eyes were closed and open, respectively. The responses at ~ 10 and ~ 14 s correspond to eye opening and blinking, respectively. (Right) Demonstration of Stroop effects in EEG measured with a passive EES.

to a red, vertical stripe that spans from 10 to 300 Hz (32).

To demonstrate EMG recording in a mode in which conventional devices are particularly ill suited, an EES mounted on the throat can monitor muscle activity, noninvasively, during speech (fig. S5A) (27). Here, recordings collected during vocalization of four words (“up,” “down,” “left,” and “right”), repeated 10 times each (fig. S6) exhibit distinctive patterns, as in Fig. 4D. Measurements from another set of words (“go,” “stop,” and “great”) (figs. S5B and S7) suggest sufficient structure in the signals for recognizing a vocabulary of words. These capabilities create opportunities for EES-based human/machine interfaces. As an example, dynamic time-warping pattern-recognition algorithms applied to throat-based EMG data (Fig. 4D) enable control of a computer strategy game (Sokoban), as illustrated in Fig. 4E. The classifications occur in less than 3 s on a dual-core personal computer running codes in MATLAB (MathWorks, Natick, MA), with an accuracy of >90% (fig. S8).

As a human/machine interface, EEG data offer additional promise. EES mounted on a region of the forehead that is first prepared by exfoliating the stratum corneum with Scotch tape yields reproducible, high-quality results, as demonstrated in alpha rhythms recorded from awake subjects with their eyes closed (fig. S9A) (27). The expected feature at ~10 Hz appears clearly in the Fourier-transformed data of Fig. 4F, left. The spectrogram of Fig. 4F, center, shows similar signatures. This activity disappears when the eyes are open. The signal-to-noise ratios are comparable with those obtained in otherwise identical experiments that used conventional, rigid bulk electrodes with conductive coupling gels. In further demonstrations, EEG measured with EES reveals well-known cognitive phenomena such as the Stroop effect (33, 34). In these experiments, subjects randomly presented with congruent or incongruent (fig. S9B) colored words whisper the color (not the word) as quickly as possible. The data show that the motor responses pertaining to the whispering are manifested by two peaks at ~650 ms (congruent case) and ~1000 ms (incongruent case), as shown in Fig. 4F, right. The time delay implies that the congruent stimuli require fewer cognitive resources and are quicker to process than are the incongruent ones, which is consistent with the literature (33, 34).

Conclusions. The materials and mechanics ideas presented here enable intimate, mechanically “invisible,” tight and reliable attachment of high-performance electronic functionality with the surface of the skin in ways that bypass limitations of previous approaches. Many of the EES concepts are fully compatible with small-scale integrated circuits that can be released from ultrathin-body silicon-on-wafer substrates. For long-term use, materials and device strategies to accommodate the continuous efflux of dead cells from the surface of the skin and the processes of transpiration will be needed.

References and Notes

- H. Berger, *Arch. Psychiatr. Nervenkr.* **87**, 527 (1929).
- C. D. Hardyck, L. F. Petrinovich, D. W. Ellsworth, *Science* **154**, 1467 (1966).
- E. J. Fox, R. Melzack, *Pain* **2**, 141 (1976).
- J. G. Webster, Ed., *Medical Instrumentation: Application and Design* (Wiley, New York, 2009), pp. 189–240.
- A. Searle, L. Kirkup, *Physiol. Meas.* **21**, 271 (2000).
- P. Griss, H. K. Tolvanen-Laakso, P. Meriläinen, G. Stemme, *IEEE Trans. Biomed. Eng.* **49**, 597 (2002).
- L. M. Yu, F. E. H. Tay, D. G. Guo, L. Xu, K. L. Yap, *Sens. Actuators A Phys.* **151**, 17 (2009).
- B. Gerde, S. Karlsson, S. Day, M. Djupsjöbacka, in *Modern Techniques in Neuroscience*, U. Windhorst, H. Johansson, Eds. (Springer Verlag, Berlin, 1999), pp. 705–755.
- J. R. Ives, S. M. Mirsattari, D. Jones, *Clin. Neurophysiol.* **118**, 1633 (2007).
- T. Sekitani *et al.*, *Science* **321**, 1468 (2008).
- S. C. B. Mannsfeld *et al.*, *Nat. Mater.* **9**, 859 (2010).
- K. Takei *et al.*, *Nat. Mater.* **9**, 821 (2010).
- D.-H. Kim *et al.*, *Science* **320**, 507 (2008).
- R.-H. Kim *et al.*, *Nat. Mater.* **9**, 929 (2010).
- M. Kubo *et al.*, *Adv. Mater. (Deerfield Beach Fla.)* **22**, 2749 (2010).
- M. Gonzalez *et al.*, *Microelectron. Reliab.* **48**, 825 (2008).
- S. P. Lacour, J. Jones, S. Wagner, T. Li, Z. Suo, *Proc. IEEE* **93**, 1459 (2005).
- C. Keplinger, M. Kaltenbrunner, N. Arnold, S. Bauer, *Proc. Natl. Acad. Sci. U.S.A.* **107**, 4505 (2010).
- L. Hu *et al.*, *Nano Lett.* **10**, 708 (2010).
- O. Kuwazuru, J. Saotthong, N. Yoshikawa, *Med. Eng. Phys.* **30**, 516 (2008).
- M. Geerligts *et al.*, *J. Biomech.* **44**, 1176 (2011).
- C. Paillet-Mattei, S. Bec, H. Zahouani, *Med. Eng. Phys.* **30**, 599 (2008).
- <http://dermatology.about.com/cs/skinanatomy/a/anatomy>.
- V. Arumugam, M. D. Naresh, R. Sanjeevi, *J. Biosci.* **19**, 307 (1994).
- L. Tchivaleva *et al.*, in *Skin Roughness Assessment. New Developments in Biomedical Engineering*, D. Campolo, Ed. (Intech, www.intechopen.com/download/pdf/pdfs_id/9090, 2010).
- K.-P. Wilhelm, P. Elsner, E. Berardesca, *Bioengineering of the Skin: Skin Surface Imaging and Analysis* (CRC, Boca Raton, 1997).
- Materials and methods are available as supporting material on Science Online.
- D.-H. Kim *et al.*, *Proc. Natl. Acad. Sci. U.S.A.* **105**, 18675 (2008).
- A. Kaneko, N. Asai, T. Kanda, *J. Hand Ther.* **18**, 421, quiz 425 (2005).
- K. C. Cheung, P. Renaud, H. Tanila, K. Djupsund, *Biosens. Bioelectron.* **22**, 1783 (2007).
- M. Irimia-Vladu *et al.*, *Adv. Funct. Mater.* **20**, 4069 (2010).
- L. Sörnmo, P. Laguna, *Bioelectrical Signal Processing in Cardiac and Neurological Applications* (Elsevier, Amsterdam, 2005).
- J. R. Stroop, *J. Exp. Psychol.* **18**, 643 (1935).
- O. Spreen, E. A. Straus, *Compendium of Neuropsychological Tests: Administration, Norms and Commentary* (Oxford Univ. Press, New York, 2006).

Acknowledgments: This material is based on work supported by a National Security Science and Engineering Faculty Fellowship and a grant from the Air Force Research Laboratory. The manufacturing techniques were developed with support from the National Science Foundation (NSF) under grant CMMI 07-49028 and used facilities at the Materials Research Laboratory and Center for Microanalysis of Materials at the University of Illinois at Urbana-Champaign, supported by the U.S. Department of Energy, Division of Materials Sciences under awards DE-FG02-07ER46471 and DE-FG02-07ER46453. N.L. acknowledges support from a Beckman Institute postdoctoral fellowship. Y.H. acknowledges NSF grants ECCS-0824129 and OISE-1043143. We thank K. Shenoy and R. Nuzzo for useful discussions. One or more provisional patents are being filed on this work. J.A.R. is a co-founder and equity holder in the company MC10, which pursues the commercialization of biointegrated devices.

Supporting Online Material

www.sciencemag.org/cgi/content/full/333/6044/838/DC1

Materials and Methods

Figs. S1 to S17

References (35–40)

Movies S1 and S2

28 March 2011; accepted 10 June 2011

10.1126/science.1206157

A Highly Conserved Neutralizing Epitope on Group 2 Influenza A Viruses

Damian C. Ekiert,^{1*} Robert H. E. Friesen,^{2*} Gira Bhabha,¹ Ted Kwaks,² Mandy Jongeneelen,² Wenli Yu,¹ Carla Ophorst,² Freck Cox,² Hans J.W.M. Korse,² Boerries Brandenburg,² Ronald Vogels,² Just P.J. Brakenhoff,² Ronald Kompier,²† Martin H. Koldijk,² Lisette A.H.M. Cornelissen,³ Leo L. M. Poon,⁴ Malik Peiris,⁴ Wouter Koudstaal,²‡ Ian A. Wilson,^{1,5}‡ Jaap Goudsmit²

Current flu vaccines provide only limited coverage against seasonal strains of influenza viruses. The identification of V_H1-69 antibodies that broadly neutralize almost all influenza A group 1 viruses constituted a breakthrough in the influenza field. Here, we report the isolation and characterization of a human monoclonal antibody CR8020 with broad neutralizing activity against most group 2 viruses, including H3N2 and H7N7, which cause severe human infection. The crystal structure of Fab CR8020 with the 1968 pandemic H3 hemagglutinin (HA) reveals a highly conserved epitope in the HA stalk distinct from the epitope recognized by the V_H1-69 group 1 antibodies. Thus, a cocktail of two antibodies may be sufficient to neutralize most influenza A subtypes and, hence, enable development of a universal flu vaccine and broad-spectrum antibody therapies.

Influenza viruses cause millions of cases of severe illness each year, thousands of deaths, and considerable economic losses. Currently, two main countermeasures are used against flu. First, small-molecule inhibitors of the neuraminidase surface glycoprotein and the viral ion channel M2 have been widely used and proven to be

quite effective against susceptible strains (1). However, resistance to these antivirals has reduced their effectiveness, and mutations associated with oseltamivir and amantadine are widespread (2–4). The second main countermeasure is vaccination. Current vaccines that are based on inactivated viruses elicit a potent immune response

Our substrate material, whose trade name Ecoflex® appears in the SOM, was purchased from the vendor Smooth-On. Our paper identified BASF, who makes a polymer with an identical name, Ecoflex®, as the chemical supplier. We recently discovered that these two materials are different. The Ecoflex® from Smooth-On is described as a 'modified silicone'. The Ecoflex® from BASF is described as a 'modified polyester'. The paper should be corrected by replacing '(BASF, Ludwigshafen, Germany)' with '(Smooth-On, Easton, USA)', and 'modified polyester' with 'modified silicone'.



www.sciencemag.org/cgi/content/full/333/6044/838/DC1

Supporting Online Material for

Epidermal Electronics

Dae-Hyeong Kim, Nanshu Lu, Rui Ma, Yun-Soung Kim, Rak-Hwan Kim, Shuodao Wang, Jian Wu, Sang Min Won, Hu Tao, Ahmad Islam, Ki Jun Yu, Tae-il Kim, Raed Chowdhury, Ming Ying, Lizhi Xu, Ming Li, Hyun-Joong Chung, Hohyun Keum, Martin McCormick, Ping Liu, Yong-Wei Zhang, Fiorenzo G. Omenetto, Yonggang Huang, Todd Coleman, John A. Rogers*

*To whom correspondence should be addressed. E-mail: jrogers@uiuc.edu

Published 12 August 2011, *Science* **333**, 838 (2010)
DOI: 10.1126/science.1206157

This PDF file includes:

Materials and Methods

Figs. S1 to S17

References (35–40)

Other Supporting Online Material for this manuscript includes the following:
(available at www.sciencemag.org/cgi/content/full/333/6044/838/DC1)

Movies S1 and S2

Supporting Online Material

S1. Estimation of driving forces for interfacial delamination between devices and skin

Fracture mechanics of a linear elastic bilayer system (33) gives a steady-state driving force of $G = \frac{1}{2}Eh\varepsilon^2$ for interface delamination between a thin film of Young's modulus E and thickness h and a thick substrate under uniform tensile strain ε . For tensile/compressive strain of 1%, the driving forces for interface delamination of 1 mm-thick sheet of silicon ($E = 180$ GPa) and 75 μm -thick sheet of polyimide ($E = 4$ GPa) are 9×10^3 J/m² and 15 J/m², respectively. For EES ($E = 150$ kPa, $h = 30$ μm), the driving force is only 2.25×10^{-4} J/m², which is more than four orders of magnitude lower than silicon or polyimide based devices.

S2. Sample preparation for confocal microscopy

To prepare samples for confocal microscopy, we stained the polymers and the pig skin with fluorescent dyes having distinct excitation and emission bands, as shown in Fig. S2A. Alexa 488 (Invitrogen[®]) was used to stain the silicone substrate. Ten grams of Alexa 488 powder was first dissolved in 300 μl DMSO (Dimethyl Sulfoxide). Next, 1 μl of the 488-DMSO solution was diluted by 1 ml toluene and 100 μl of the resulting 488-DMSO-toluene solution was added to 2 ml Part A pre-polymer of 0030 Ecoflex[®]. A magnetic stir bar was used to facilitate mixing, for 1 hour. We next added 2 ml Part B pre-polymer of Ecoflex and further mixed for 5

minutes. Spin coating this pre-polymer mixture at 3000 rpm onto a water-soluble PVA substrate and curing at room temperature for 4 hours and then at 70°C for 2 hours completed the preparation of the stained silicone. Alexa 647 (Invitrogen[®]) was used to stain a film of polyimide, patterned into the shape of representative electronic circuits with FS or FS-island designs. For the polyimide we dissolved ten grams of Alexa 647 powder into 300 μ l DMSO. We then added 1 μ l 647-DMSO to 1 ml NMP (N-Methylpyrrolidone) and mixed 10 μ l of the resulting 647-DMSO-NMP solution into 1 ml of polyimide pre-polymer. As before, we used a magnetic stir bar to mix for 1 hour. Spin coating at 4000 rpm onto a PMMA coated Si wafer and baking at 250°C in glove box for 1 hour completed the preparation. Patterning the PI was accomplished by photolithography and dry etching. The final step involved transfer-printing the polyimide structure onto a silicone (Ecoflex[®])-coated PVA substrate.

To stain the pig skin, we first mixed 10 gram FM 1-43FX (Invitrogen[®]) into 300 μ l DMSO. We then diluted 1 μ l FM-DMSO solution with 1 ml 1x PBS (Phosphate Buffered Saline). We rinsed the pig skin by 1x PBS thoroughly. Applying a drop of the FM-DMSO-PBS solution onto the skin surface and waiting for 10 minutes produced the desired stain. Rinsing with 1x PBS removed excess dye. Fluorescent EES was then applied to stained pig skin sample by placing the device side against the surface of the skin and then gently spraying 1xPBS to dissolve away the PVA backing layer.

During imaging, a 488 nm laser was used to excite both Alexa 488 and FM 1-43. Alexa 647 was excited by a 639 nm laser. Three tracks were created for the silicone substrate (Alexa 488, blue), polyimide (Alexa 647, red), and pig skin (FM 1-43FX, blue and green) respectively. In-plane as well as thickness direction resolution was \sim 1 μ m. Three dimensional confocal

scanning results from bare pig skin and FS-island EES on pig skin appear in Figs. S2B and S2C, respectively.

S3. Macroscopic mechanics models for interfacial delamination under tension/compression

The driving force for interfacial delamination between a PDMS film and a silicone sheet subject to tensile strain ε in the silicone can be obtained analytically as

$$G = \frac{\bar{E}_{\text{PDMS}} h_{\text{PDMS}} \bar{E}_{\text{silicone}} h_{\text{silicone}} \varepsilon^2}{2 \left(1 - \frac{\bar{E}_{\text{PDMS}} h_{\text{PDMS}}}{\bar{E}_{\text{PDMS}} h_{\text{PDMS}} + \bar{E}_{\text{silicone}} h_{\text{silicone}}} \frac{L_{\text{PDMS}}}{L_{\text{silicone}}} \right)^2} \times \frac{\bar{E}_{\text{PDMS}} h_{\text{PDMS}}^3 + \bar{E}_{\text{silicone}} h_{\text{silicone}}^3}{\left(\bar{E}_{\text{PDMS}} h_{\text{PDMS}}^2 - \bar{E}_{\text{silicone}} h_{\text{silicone}}^2 \right)^2 + 4 \bar{E}_{\text{PDMS}} h_{\text{PDMS}} \bar{E}_{\text{silicone}} h_{\text{silicone}} (h_{\text{PDMS}} + h_{\text{silicone}})^2} \quad (\text{S1})$$

where \bar{E} , h and L are the plane-strain modulus, thickness and length of the corresponding layers. Equation (S1) is an extension of the steady-state driving force for interfacial delamination of a linear elastic bilayer to account for the finite lengths of the PDMS film and silicone sheet. Finite element modeling (FEM) has been used to calculate the interfacial crack tip energy release rate. The critical delamination strain is obtained at the point where the driving force for interfacial delamination reaches the adhesion energy $\gamma_{\text{PDMS/silicone}}$ between PDMS and silicone. For 50:1 and 30:1 PDMS, the adhesion energies are measured to be 250 mJ/m² and 50 mJ/m², respectively.

For compression in the silicone, the large pre-stretch used in experiments, prevents Euler-type buckling (to an arch shape). Therefore, increasing the compression induced in this manner eventually leads to wrinkling of the PDMS on silicone. This behavior is similar to surface

wrinkling of a semi-infinite solid subject to compression parallel to the surface (35), but it is different in the following three aspects:

- 1) It involves two materials (PDMS and silicone) such that the continuity of displacements and stress tractions must be enforced;
- 2) Both layers have finite thickness, and cannot be modeled as semi-infinite solids;
- 3) Silicone has a large pre-stretch, which is not completely released during compression.

These features give the critical strain for wrinkling determined from the eigenvalue of a 8*8 matrix. For a semi-infinite solid, the critical strain for wrinkling degenerates to the prior analytical results (36).

S4. Microscopic mechanics models for contact between EES and skin

Microscopic mechanics models are developed to study contact between EES and skin, particularly on the effects of skin roughness, and device thickness and size. The skin morphology can be represented by a sinusoidal form $y(x) = h_{\text{rough}} \left[1 + \cos(2\pi x / \lambda_{\text{rough}}) \right] / 2$ with skin roughness amplitude h_{rough} and wavelength λ_{rough} . For non-conformal contact between EES and skin, EES does not follow the skin morphology and remains flat, which gives the total energy $\bar{U}_{\text{non-conformal}} = 0$. For conformal contact, both EES and skin deform such that the total displacement is $y(x)$. The displacements of EES and skin surface can be represented by $w(x) = h \left[1 + \cos(2\pi x / \lambda_{\text{rough}}) \right] / 2$ and $u_z(x) = (h_{\text{rough}} - h) \left[1 + \cos(2\pi x / \lambda_{\text{rough}}) \right] / 2$, respectively, where the maximum deflection h of EES is to be determined.

The total energy (*per unit length* along the wavelength direction) for conformal contact is

$\bar{U}_{\text{conformal}} = \bar{U}_{\text{bending}} + \bar{U}_{\text{skin}} + \bar{U}_{\text{adhesion}}$, where the bending energy of EES is

$\bar{U}_{\text{bending}} = (1/\lambda_{\text{rough}}) \int_0^{\lambda_{\text{rough}}} (\bar{EI}_{\text{EES}}/2)(w'')^2 dx = \pi^4 \bar{EI}_{\text{EES}} h^2 / \lambda_{\text{rough}}^4$, the elastic energy of skin is

$\bar{U}_{\text{skin}} \approx \pi \bar{E}_{\text{skin}} (h_{\text{rough}} - h)^2 / (16\lambda_{\text{rough}})$ (37), and the interfacial adhesion energy is

$\bar{U}_{\text{adhesion}} = -\gamma \int_0^{\lambda_{\text{rough}}} \sqrt{1+(w')^2} dx \approx -\gamma [1 + \pi^2 h^2 / (4\lambda_{\text{rough}}^2)]$, where γ , \bar{EI}_{EES} , \bar{E}_{skin} are the effective

work of adhesion, effective bending stiffness of EES, and the plane-strain modulus of the skin,

respectively. Minimization of the total energy then gives analytically

$$h = \bar{E}_{\text{skin}} h_{\text{rough}} / (16\pi^3 \bar{EI}_{\text{EES}} / \lambda_{\text{rough}}^3 + \bar{E}_{\text{skin}}).$$

Conformal contact requires $\bar{U}_{\text{conformal}} < \bar{U}_{\text{non-conformal}}$, which gives approximately, when

$$\lambda_{\text{rough}} > \sim 3h_{\text{rough}}$$

$$\frac{\pi \bar{E}_{\text{skin}} h_{\text{rough}}^2}{\gamma \lambda_{\text{rough}}} < 16 + \frac{\bar{E}_{\text{skin}} \lambda_{\text{rough}}^3}{\pi^3 \bar{EI}_{\text{EES}}}. \quad (\text{S2})$$

The scaling law in Eq. (S2), which involves two dimensionless combinations of EES and skin properties, shows that EES with low bending stiffness, on smooth and soft skin with strong adhesion all promote conformal contact. For the FS-EES (Fig. 2B), $\bar{EI}_{\text{EES}} \approx 0.27 \times 10^{-9}$ N-m (SOM Section S5), $\bar{E}_{\text{skin}} \approx 130$ kPa , $\lambda_{\text{rough}} \approx 140$ μm , $\gamma \approx 0.16$ N/m (SOM Section S5), the above criterion implies that EES will achieve conformal contact with skin when the skin roughness is smaller than ~ 56 μm . This result is consistent with contact observed in Fig. 2E (roughness in the range of 5~20 μm).

For the FS-island EES (Fig. S1F), the device is much thicker (Au 0.5 μm – PI 1.2 μm – Au 0.2 μm – PI 1.2 μm) and larger (500 μm ×500 μm) than the FS strips (0.5 μm thick, 100 μm wide). For 400 μm spacing between adjacent islands (Fig. S1D), the effective bending stiffness is $\overline{EI}_{\text{EES}} \approx 1.6 \times 10^{-9}$ N-m from FEM, and the effective work of adhesion is $\gamma \approx 0.14$ N/m (SOM Section S5). The criterion above implies that EES loses conformal contact once the skin roughness exceeds 27 μm , which is consistent with partial contact observed in the experiments for the range of skin roughness 20~50 μm (Fig. S2C). If the thickness of the island is decreased to the same as in the FS-EES design, the island-FS EES loses conformal contact with skin rougher than 48 μm , compared to 56 μm for FS-EES. In comparison, the smaller thickness and area fraction of FS-EES promote conformal contact.

For the FS-EES design, the effect of device thickness is studied by changing thicknesses of all layers proportionally. Let h_{device} denote the total thickness of device. Figure S10A shows that, for FS made of Au-PI as in experiments (red curve), the skin roughness for conformal contact decreases from ~56 μm to ~30 μm as the device thickness increases by 8 times. If all elastic moduli are proportionally reduced by 1000 times (blue curve), FS-EES would have conformal contact with much rougher skin. Therefore, thinner, softer devices promote conformal contact between EES and skin.

The thickness and modulus of the device and the skin roughness also play important roles on the comfort, or ‘wearability’, of EES. The contact pressure at the EES-skin interface is obtained analytically as (37)

$$\sigma_{\text{contact-global}} = \frac{8\pi^4 \bar{E}_{\text{skin}} h_{\text{rough}}}{16\pi^3 \lambda_{\text{rough}} + \frac{\bar{E}_{\text{skin}} \lambda_{\text{rough}}^4}{EI_{\text{EES}}}} \cos \frac{2\pi x}{\lambda_{\text{rough}}}. \quad (\text{S3})$$

Figure S10B (blue curve) shows the contact pressure between the FS-EES and skin of average roughness ($h_{\text{rough}} = 30\mu\text{m}$) for EES with device thickness of $0.5 \mu\text{m}$. The maximum contact pressure is only 12.5 kPa, which is below the human skin sensitivity ($\sim 20\text{kPa}$ (29)) and therefore does not induce discomfort. From Eq. (S3), it is obvious that softer device materials will give smaller contact pressure.

Figure S11 illustrates the mechanics model to determine the gap width a along the edges of EES. Since FS thickness h_{device} ($\sim 1 \mu\text{m}$) is much smaller than that of the skin ($\sim 1 \text{mm}$) and the silicone ($\sim 30 \mu\text{m}$) and the FS strip width ($\sim 100 \mu\text{m}$), the FS between the skin and silicone is analogous to inserting a rigid wedge of uniform thickness h_{device} at the skin/ silicone interface, leading to an interfacial crack (38). The interfacial crack tip energy release rate is (39)

$$G \approx \frac{(\bar{E}_{\text{skin}} + \bar{E}_{\text{silicone}}) h_{\text{device}}^2}{16\pi a}. \quad (\text{S4})$$

The gap width a is obtained by G reaching the work of adhesion $\gamma_{\text{silicone/skin}}$ as

$$a \approx \frac{(\bar{E}_{\text{skin}} + \bar{E}_{\text{silicone}}) h_{\text{device}}^2}{16\pi \gamma_{\text{silicone/skin}}}, \quad (\text{S5})$$

which has been verified by FEM for the range of FS thickness in experiments.

The stress distribution $\sigma_{\text{contact-local}}$ over FS width is obtained analytically (38), and is shown schematically in Fig. S11. The total force on FS strip is the integration of this $\sigma_{\text{contact-local}}$

and $\sigma_{\text{contact-global}}$ in Eq. (S3) over FS strip width, $F_{\text{total}} = \int_{\text{FS width}} (\sigma_{\text{contact-global}} + \sigma_{\text{contact-local}}) dx$, which has an average of -0.1 N/m for skin with $h_{\text{rough}} = 15 \mu\text{m}$ and $\lambda_{\text{rough}} = 140 \mu\text{m}$.

S5. Effective work of adhesion between EES and skin, and effective bending stiffness of EES

The effective work of adhesion between EES and skin is given by

$$\gamma = \alpha \gamma_{\text{device/skin}} + (1 - \alpha) \gamma_{\text{silicone/skin}}, \quad (\text{S6})$$

where α is the area fraction of devices, and $\gamma_{\text{device/skin}}$ and $\gamma_{\text{silicone/skin}}$ are the work of adhesion for device-skin and silicone-skin interfaces, respectively. Since adhesion between device (Au) and skin is very weak, Eq. (S6) is simplified to $\gamma \approx (1 - \alpha) \gamma_{\text{silicone/skin}}$. For the experimental value of $\gamma_{\text{silicone/skin}} = 0.2 \text{ N/m}$ measured by the rod-rolling set-up described in (40), the effective work of adhesion is $\gamma \approx 0.16 \text{ N/m}$ for the FS-EES ($\alpha \approx 22.5\%$) and $\gamma \approx 0.14 \text{ N/m}$ for the island-plus-serpentine EES ($\alpha \approx 30.9\%$).

Similarly, for FS strips distributed over the entire surface of FS-EES electronics, the effective bending stiffness of EES is given by

$$\overline{EI}_{\text{EES}} = \alpha \overline{EI}_{\text{device}} + (1 - \alpha) \overline{EI}_{\text{silicone}}, \quad (\text{S7})$$

where $\overline{EI}_{\text{silicone}} = \overline{E}_{\text{silicone}} h_{\text{silicone}}^3 / 12$ is the bending stiffness of silicone ($\overline{E}_{\text{silicone}} = 65 \text{ kPa}$ and $h_{\text{silicone}} = 30 \mu\text{m}$ are the plane-strain modulus and thickness of silicone, respectively), and the

bending stiffness for silicone with device is $\overline{EI}_{\text{device}} = \sum_{i=1}^3 \overline{E}_i h_i \left[\left(b - \sum_{j=1}^i h_j \right)^2 + \left(b - \sum_{j=1}^i h_j \right) h_i + \frac{1}{3} h_i^2 \right]$

(where $b = \sum_{i=1}^3 \overline{E}_i h_i \left(\sum_{j=1}^i h_j - \frac{1}{2} h_i \right) / \sum_{i=1}^3 \overline{E}_i h_i$; $\overline{E}_1 = \overline{E}_{\text{silicone}}$, $h_1 = h_{\text{silicone}}$; $\overline{E}_2 = 2.8\text{GPa}$, $h_2 = 0.3\mu\text{m}$

are the plane-strain modulus and thickness for PI, respectively; and $\overline{E}_3 = 97\text{GPa}$, $h_3 = 0.2\mu\text{m}$ for Au). For $\alpha \approx 22.5\%$ from Fig. 2B, Eq. (S7) gives the effective bending stiffness 0.27×10^{-9} N-m, which agrees reasonably well with 0.30×10^{-9} N-m obtained by FEM.

S6. Sample fabrication of an FS-EES active EP sensor

The sample fabrication began with high temperature diffusion doping to define low resistance source and drain area for Ohmic contacts. Phosphorous spin-on-dopant (P509, Filmtronics, USA) was diffused at 950°C with a constant supply of the gas mixture: nitrogen:oxygen = 8:2. Transfer printing the resulting doped silicon nanomembrane to a handle wafer coated with PMMA/PI, followed by dry etching to isolate the active regions, defined silicon areas on thin PI, as shown in Fig. 3A left frame. Electron-beam evaporation of metal (Cr/Au, 50/1500Å) formed lines that connect ground and output to the sensor and that define source, drain and gate electrodes (Fig. 3A right frame and its inset for a magnified view). Depositing additional metallization for large area sensor electrodes, and connecting between different layers through vias, followed by a second transfer printing step to deliver the system to silicone-coated PVA completed the process. Attaching the output pads to an anisotropic

conductive film (ACF) provided connection to an external circuit board for data transfer, as shown in Fig. S12.

S7. General setups for all electro-physiological measurements

All electro-physiological signals were measured with three types of electrodes: the recording electrode, the reference electrode and the ground electrode (See Fig. S4A). Dry EES devices can be used for all electrode-skin contacts (i.e. recording, reference and ground electrode) as shown in Fig. S17A and Movie S2. Similar recordings, made with gels and conventional electrodes appear in Fig. S17B.

The ground electrode defines a point of zero-potential, since it is normally attached to an electrically neutral area of the subject's body, e.g. the bony area of the right ankle (ECG and EMG) or the earlobes (EEG). In this manner, the ground electrode provides a common zero-potential point for defining electric potentials in both the recording electrode and the reference electrode, which are normally attached over and across the signal source.

The potential difference between the recording electrode and the reference electrode is the electro-physiological signal that we measure. This potential is amplified by a differential amplifier (James Long Company, NY), and discretized by an analog-to-digital converter (Personal Daq/3000, IOtech, OH. See Fig. S4A). All signals are transmitted by ACF wires and cables. All test subjects were co-authors of this paper therefore no IRB (Institutional Review Board) approval was necessary.

S8. ECG measurement

The body ground electrode was a tin electrode filled with conductive gel, attached to the bony area on the right side of the subject's right ankle. The active dry EES was attached to the lower-left edge of the rib cage, near the left side of the midline of the chest. One of the electrodes on the EES was used as reference electrode, while another was recording electrode. The negative end of the AA battery that powered the EES was also connected to the body ground. The gain of the main amplifier was 10000, with a high-pass frequency (HPF) of 0.1 Hz, and a low-pass-frequency (LPF) of 100 Hz. The sampling frequency was 1000 Hz. A notch filter was applied in software to eliminate 60 Hz power line interference.

S9. EMG measurement from Leg

The active dry EES was attached at about 1/3 the distance from the knee to the ankle, on the interior side of the left leg. Other parameters were the same as those for ECG, but with HPF= 0.01 Hz and LPF= 300 Hz. Passive measurements were performed separately after recording with the EES, in otherwise exactly the same configurations. Two tin electrodes were attached in close vicinity of the EES, one on each side of it, vertically along the axis of extension of the muscle. The voltage differences between them were reported as the passive EMG.

S10. EMG measurement from Neck

The body ground electrode was attached to the right side of the subject's neck. The active dry EES was attached at the skin overlying the cricothyroid muscle. The measurement parameters were the same as those for EMG on the leg.

S11. EEG measurement from forehead (alpha rhythms and Stroop effects)

Passive dry EES of both single channel design and multi-channel design have been tested in EEG measurements. For single channel design, the body ground and reference electrodes were commercial gold electrodes without using conductive gel, attached to the subject's left and right earlobes respectively. The EES was attached to the center of the subject's forehead without applying conductive gel, after exfoliating the skin with Scotch tape. To test the multi-channel EES, one of the electrodes serves as reference electrode, while each other electrode provides a separate recording electrode. All other conditions were set up the same way as that of the single channel EES. The gain of the main amplifier was 10000, HPF= 0.01 Hz, LPF= 300 Hz. Sampling frequency was 1000 Hz. A notch filter was applied in software to eliminate 60 Hz power line interference.

S12. Simulated computer game control via neck EMG measured by EES

All computations were done in Matlab[®]. After eliminating 60 Hz interference from the raw data using a software notch filter, the feature vector associated with each utterance was generated from the spectrogram of the data, using a sliding window length of 256, overlap size of

250, and the fast-fourier transform (FFT) length of 512. Spectrograms were generated for an entire trial first, and then sliced into 750 ms intervals that correspond to the utterances of words, according to EMG onset times. These onset times were determined by an energy detecting procedure, where raw data were first sent through a high pass filter (Chebyshev type I, cutoff 70 Hz, high-pass 80 Hz), concatenated by a matched filter, and the signals were then squared. Whenever the power crossed a threshold value (typically 0.0002), a pair of onset and offset times of EMG activity was recorded.

In the original labeled dataset, there were 63 feature vectors for each of the 4 words. The metric of distance between any two feature vectors was the L1-norm (the total sum of absolute values of element-wise differences), and dynamic time warping (DTW) was used to calculate the similarity score between them. In the computer game control demonstration, the user manipulated an avatar that can move in 4 directions in the game called Sokoban. In a simulated demonstration, when the user presses a key to signify the intended direction for the avatar, a candidate feature vector is randomly drawn from the EMG feature pool for that direction, and compared with all the rest of the feature vectors in all four pools as references, in terms of DTW scores. As a result, a nearest neighbor can be found for the candidate from one of the four pools, and it will be classified as a member from this nearest neighbor's group.

The classification accuracy depends on the number of reference feature vectors available for each direction (Fig S8). We have simulated (by resampling the data pool without replacement in 100 trials) the situation where various numbers of references were randomly available from each of the four pools, and found that the classification accuracy estimated across 100 trials increased with the number of references. When 62 references in each pool were used, the

averaged accuracy could be higher than 95% for “up” and “down”, and higher than 85% for “left” and “right”. Thereby, the intended directions can be accurately classified and conveyed to the avatar, and gaming can thus be accomplished.

S13. DFT (discrete Fourier transform) coefficient

Given a vector of length N , $x[1], \dots, x[N]$, the definition of the DFT coefficients, $X(k)$, is as follows.

$$X(k) = \sum_{j=1}^N x[j] \cdot \exp\left\{-\frac{2\pi i}{N}(j-1)(k-1)\right\} \text{ where } k = 1, \dots, N$$

S14. Fatigue test

Repetitive stretching up to 1000 times with 30% tensile strain at 20 rpm shows no performance (resistance) degradation of the FS electrodes, as shown in Fig. S13.

S15. Durability test

We mounted FS-EES on the cheek (Fig. S14), chin (Fig. S15) and elbow (Fig. S16) for up to 24 hours to verify the bio-compatibility and durability of the devices. The FS-EES remained intact and no redness or inflammation in facial skin was observed after attachment to the cheek for 24 hours as shown in Fig. S14. The FS-EES attached to chin/jaw region also remained unaffected, even after the subject had lunch, as shown in Fig. S15. The EES attached to

the elbow can accommodate stretching and bending shortly after mounting, but exhibited crack after 8 hours, as shown in Fig. S16.

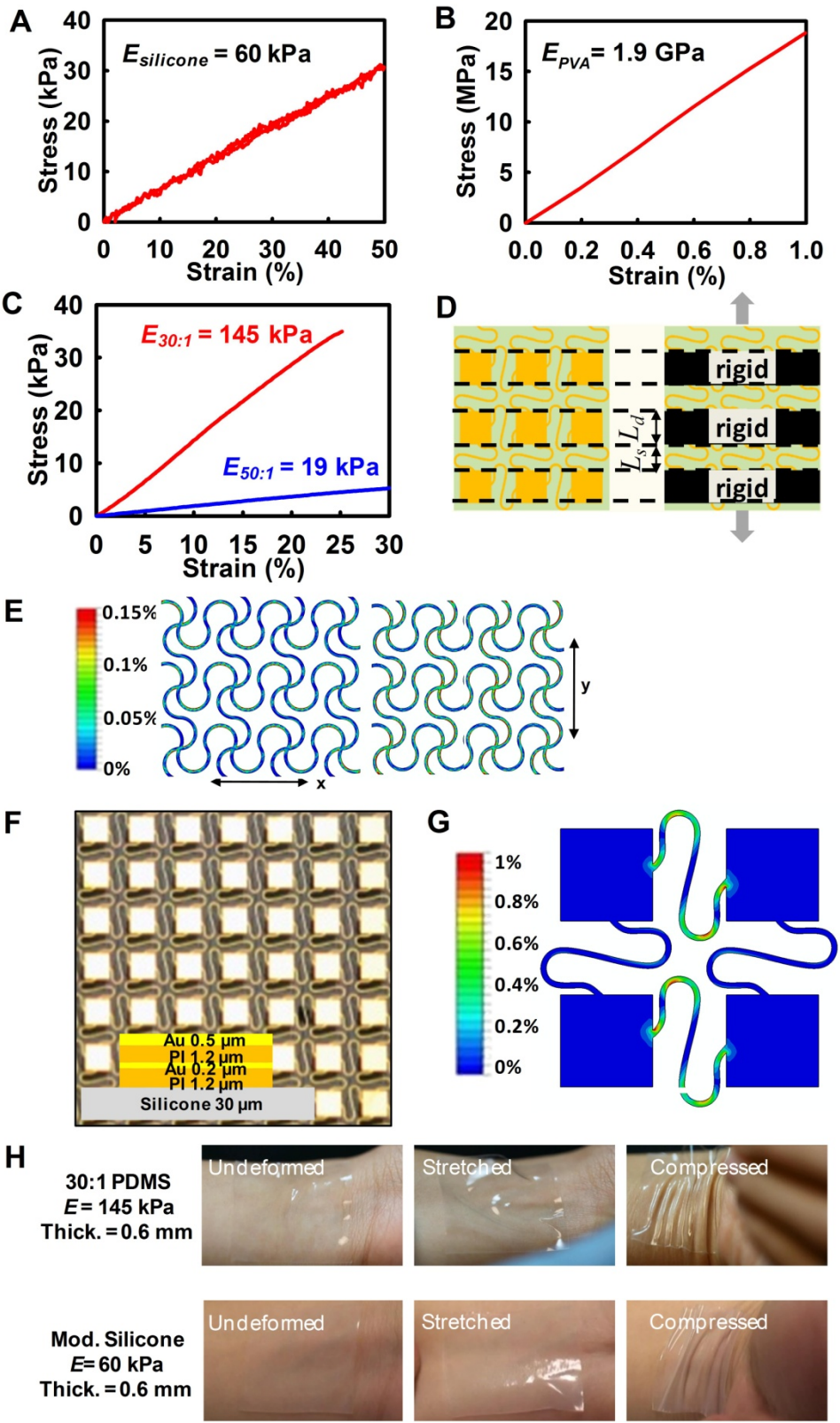


Fig. S1. (A) Uniaxial stress-strain curve for a 30 mm thick free-standing silicone film. The Young's modulus is 60 kPa. (B) Uniaxial stress-strain curve for PVA. The Young's modulus is 1.9 GPa. (C) Uniaxial stress-strain curve for 30:1 and 50:1 PDMS, with Young's moduli of 145 kPa and 19 kPa respectively. (D) Schematic illustration for a device island with size L_d and a serpentine span L_s . (E) Contour plots of maximum principle strain distributions computed by FEM, for 30% tensile strains along x (left) and y (right). The results indicate maximum principle strains of less than 0.2% in materials of the FS structures. (F) Top view and cross-sectional schematic illustrations of an FS-island sample. (G) Contour plot of strain in an island-plus-serpentine sample after stretching by 30%, computed using FEM. (H) Delamination modes of PDMS (thickness 0.6 mm; modulus 145 kPa) and silicone (thickness 0.3 mm; modulus of 60 kPa) films laminated on human wrist. In contrast, for EES devices conformal contact is maintained under extreme deformations, due simply to the action of van der Waals forces, as shown in Figs. 1C and 2C.

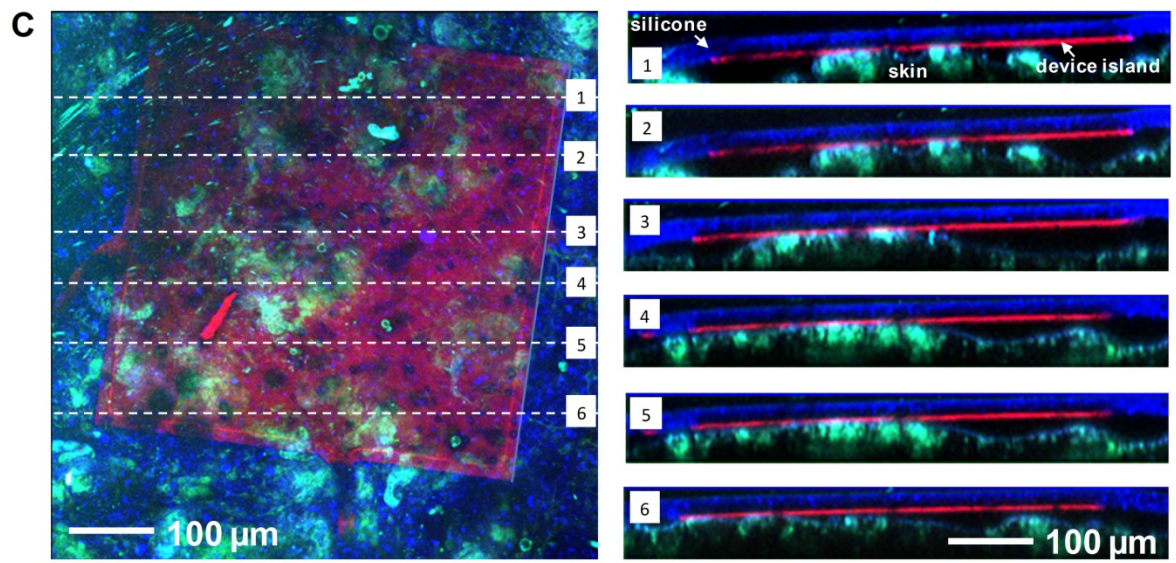
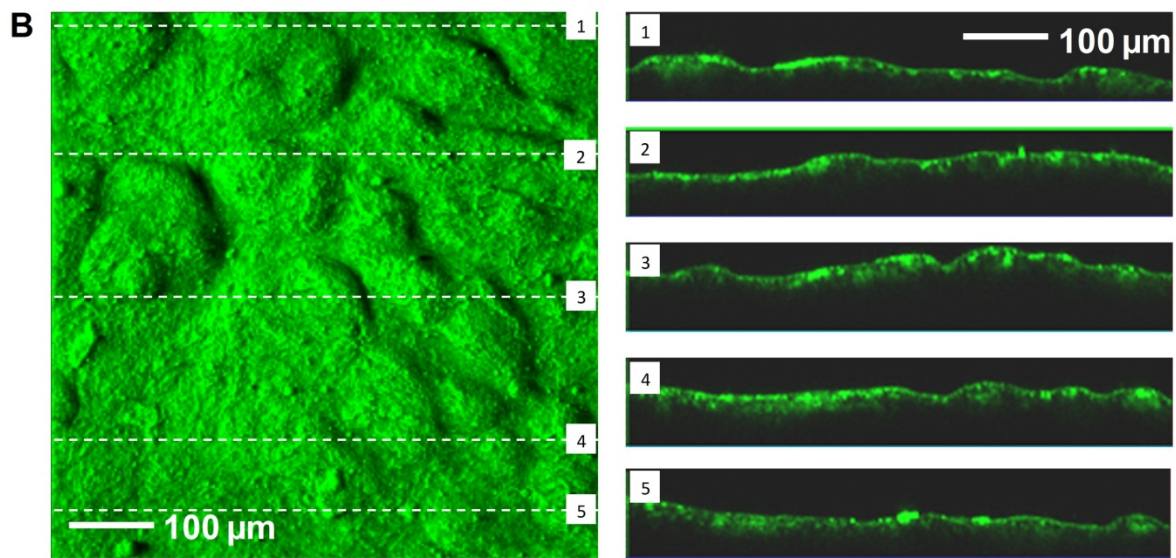
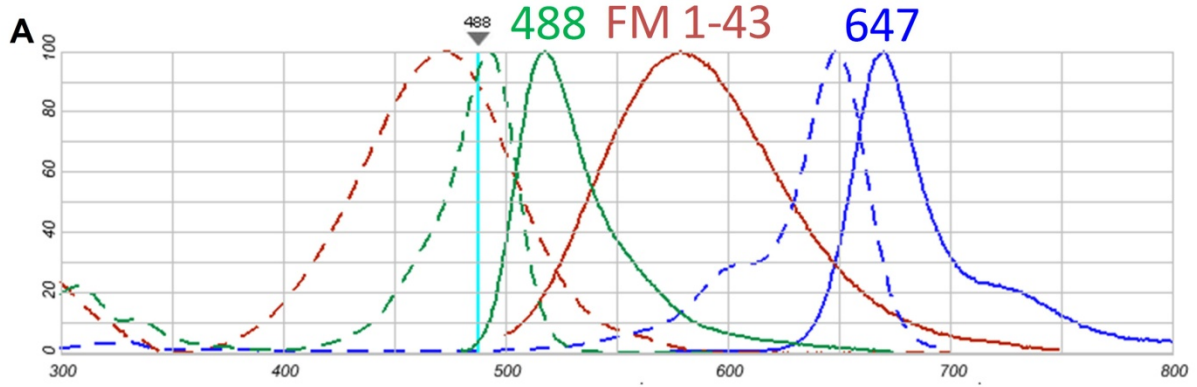


Fig. S2. (A) Excitation and emission spectrum of fluorescent dyes used for confocal microscopy. Alexa Fluor 488 is used to stain the silicone substrate and Alexa Fluor 647 is used to stain polyimide, which is patterned into the layout of electrodes. Pig skin is stained by FM 1-43FX, which labels cell membrane. (B) Top and cross-sectional views of bare pig skin. (C) Top and cross-sectional views of EES with island mounted on pig skin.

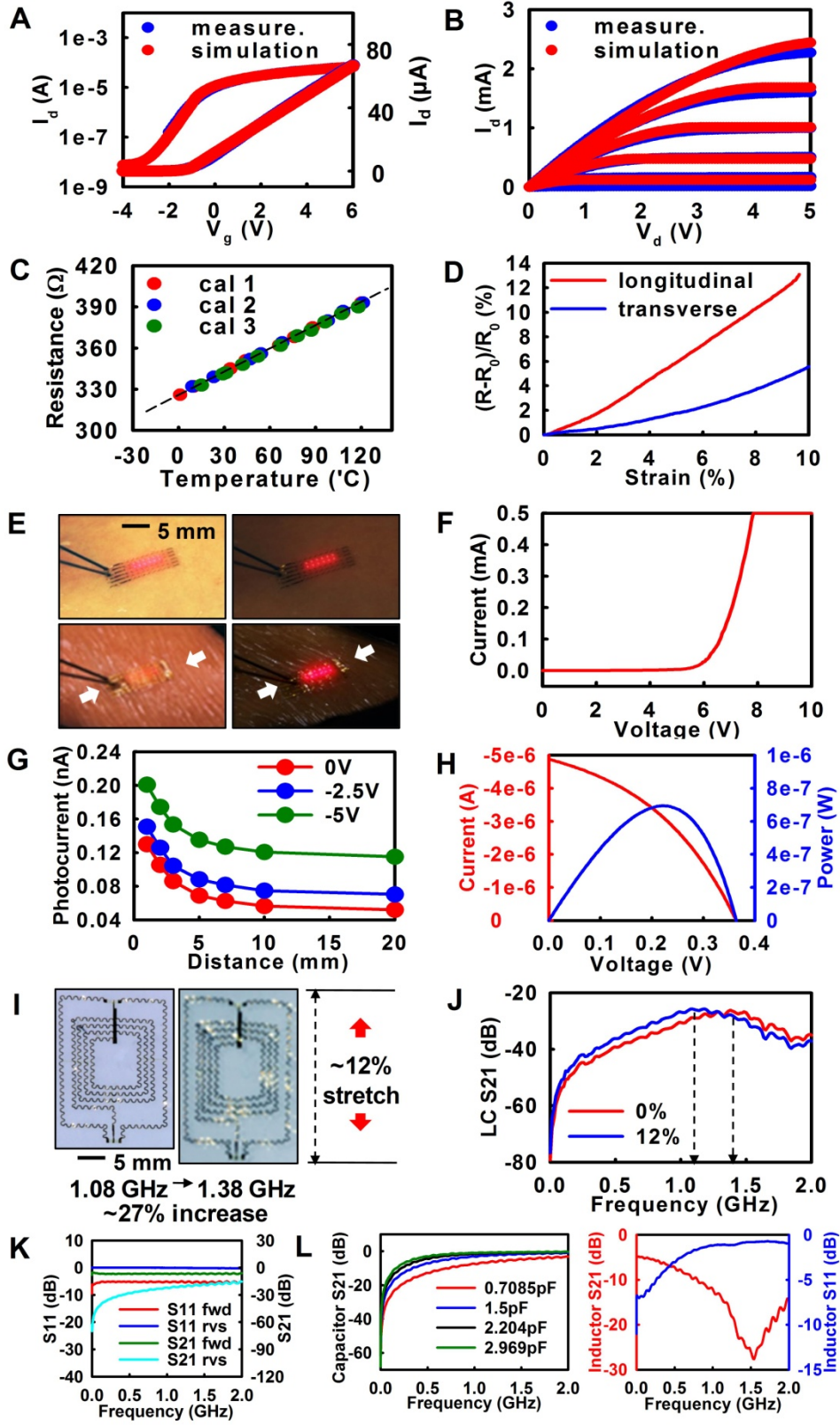


Fig. S3. (A) Transfer curve and (B) IV curve of a Si MOSFET in an FS geometry. (C) Calibration curve of a temperature sensor. (D) Percentage change in resistance of the strain gauge as a function of uniaxial tensile strain. Gauge factors for the longitudinal and transverse strain gauges are 1.3 and 0.5 respectively. (E) Proximity sensor and optical measurement system on skin using a combined LED-photodetector array with forward and reverse biases before (top frame) and after (bottom frame) deforming the skin with (left frame) and without (right frame) external illumination. (F) Current-voltage characteristics of a single LED. (G) Measured photocurrent from reverse biased diodes at different distances between the sensor and the external object. (H) Current and power from a FS Si photovoltaic cell at different voltages. (I) Images of an LC (inductor-capacitor) oscillator at 0% (left frame) and ~12% (right frame) tensile strain. (J) S₂₁ of an LC oscillator as a function of frequency. The resonant frequency changes from 1.08 GHz (0% strain) to 1.38 GHz (~12% strain) due to tensile deformation. (K) The frequency dependence of S₁₁ and S₂₁ of a RF diode. (L) The plot in the left frame shows the value of S₂₁ measured on a set of FS capacitors as a function of frequency. The plot in the right frame shows the frequency dependence of S₂₁ and S₁₁ for an FS inductor.

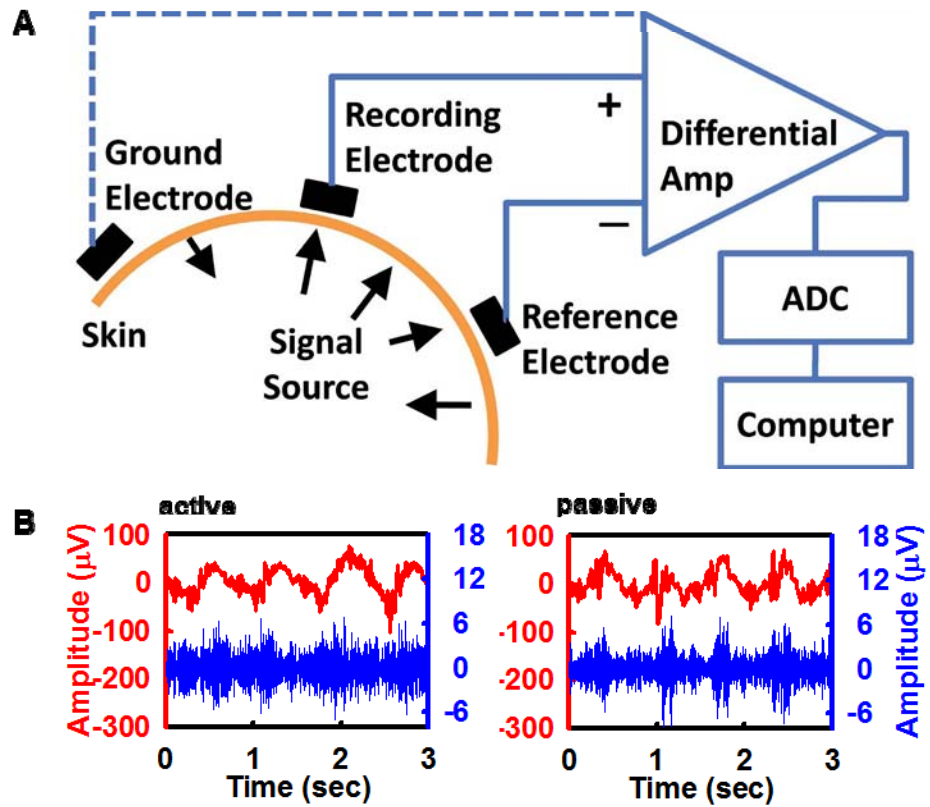


Fig. S4. (A) Schematic illustration of the general setups for all electro-physiological measurements. See SOM S7 for details. (B) Magnified view of the EMG signal of Fig. 4B. Red and blue plots correspond to raw and high-pass filtered data, respectively.

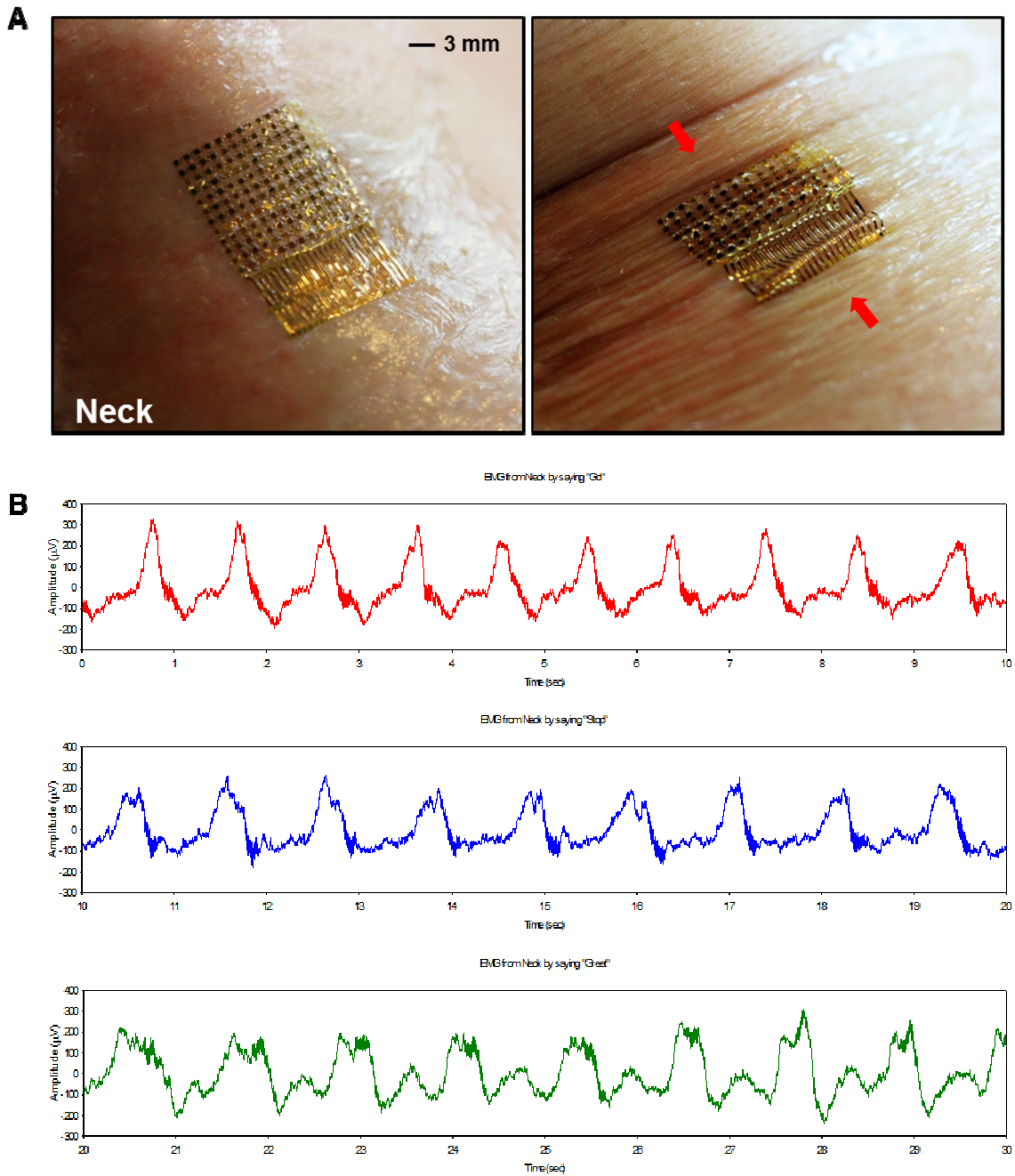


Fig. S5. (A) Images of an active EES-based EMG sensor on the neck without (left frame) and with (right frame) skin deformation. (B) Raw recordings from the neck determined using a similar sensor for different words. “Go” (top frame), “Stop” (middle frame) and “Great” (bottom frame).

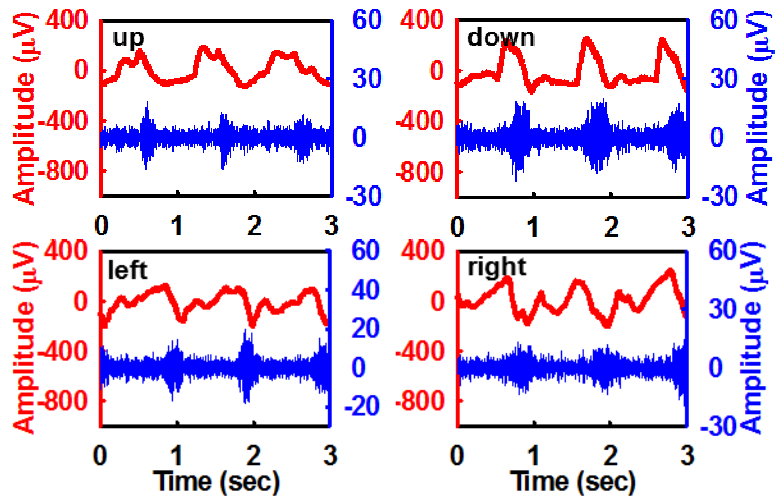


Fig. S6. EES EMG measurement from the neck for four different words, "up", "down", "left" and "right". Red and blue plots correspond to raw and high-pass filtered data, respectively.

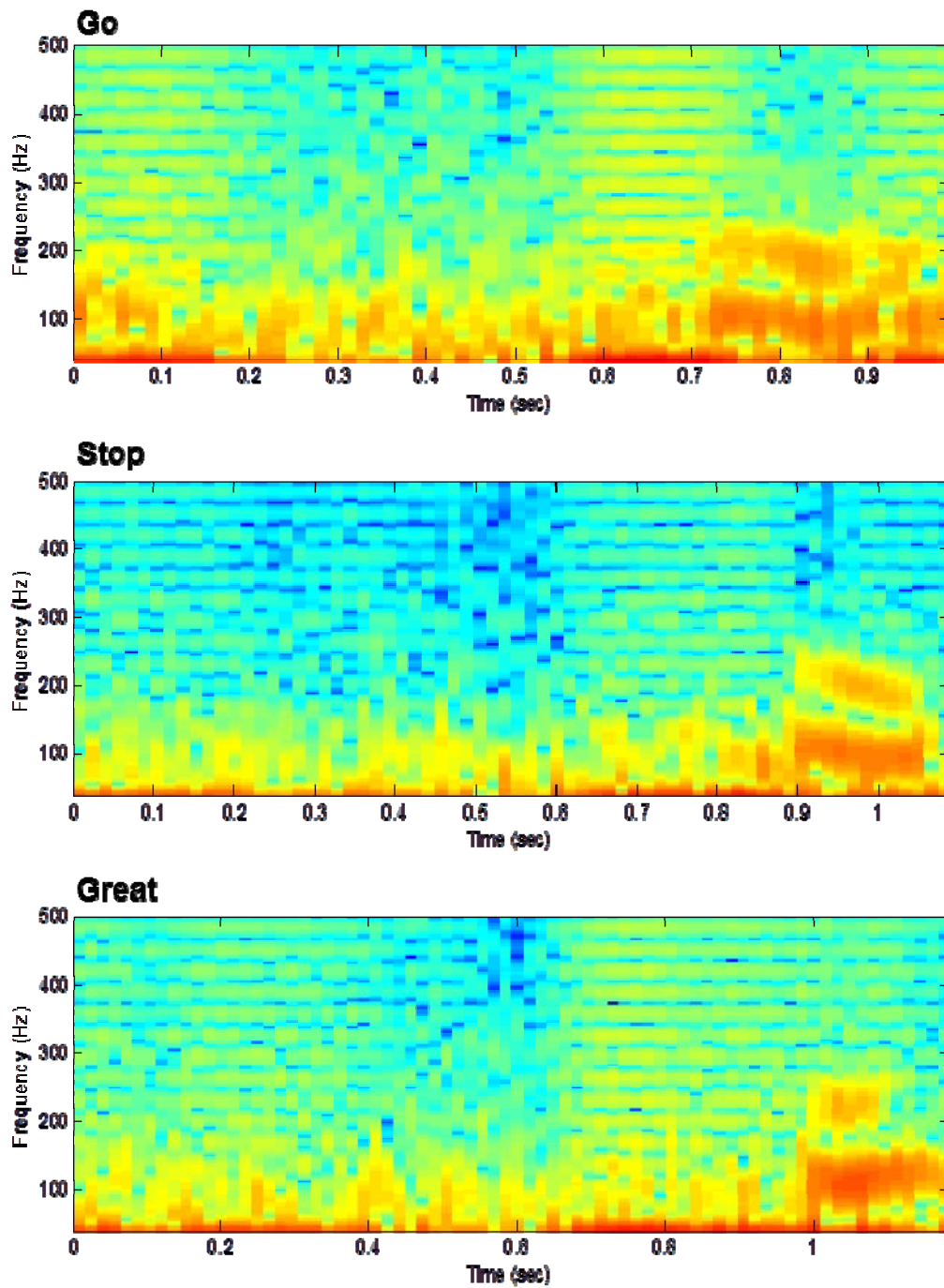


Fig. S7. Spectrograms of EES EMG measurements from the neck for three different words, “Go” (top frame), “Stop” (middle frame) and “Great” (bottom frame).

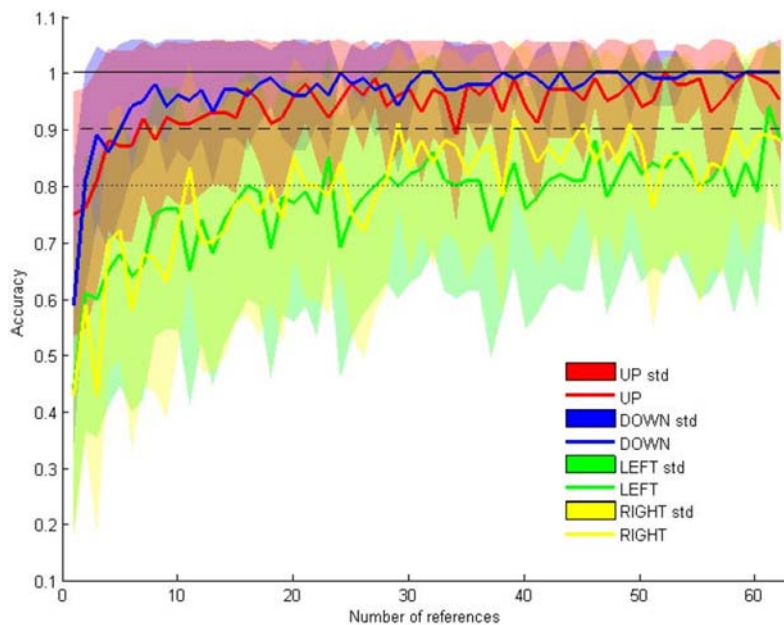


Fig. S8. Averaged classification accuracy versus the number of reference feature vectors available for classifying each direction, estimated by bootstrapping. Shaded areas indicate one standard deviation of the accuracy.

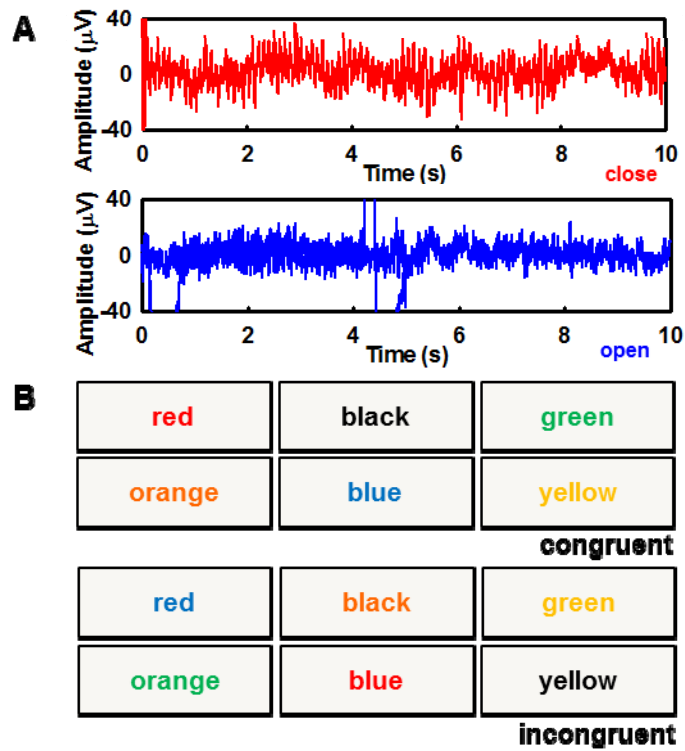


Fig. S9. (A) Recorded EEG data using a passive EES sensor with eyes closed (top frame) and eyes open (bottom frame). (B) Experimental setup for the Stroop test. When the target letter matches with its color (congruent case) the response speed is faster than the unmatched (incongruent) case.

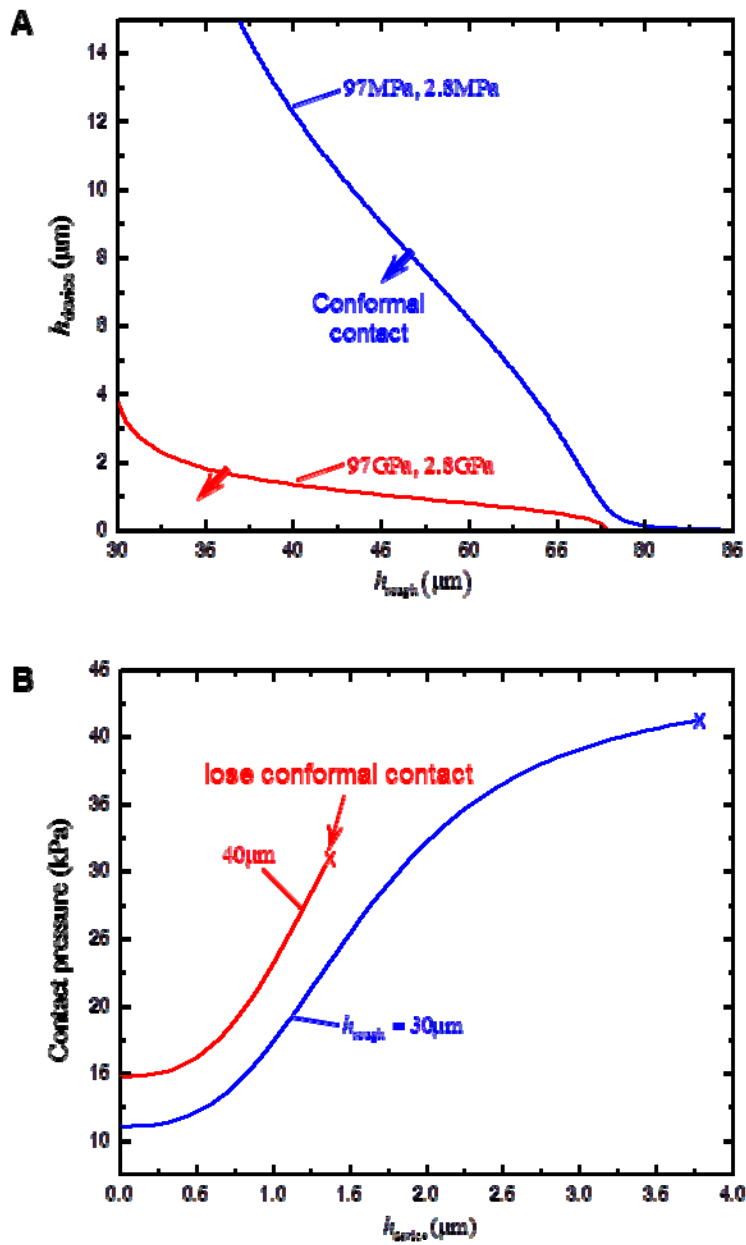


Fig. S10. (A) Conformal contact requirement for FS-EES with devices of different thickness and modulus. (B) Contact pressure between an FS-EES and skin with different roughnesses.

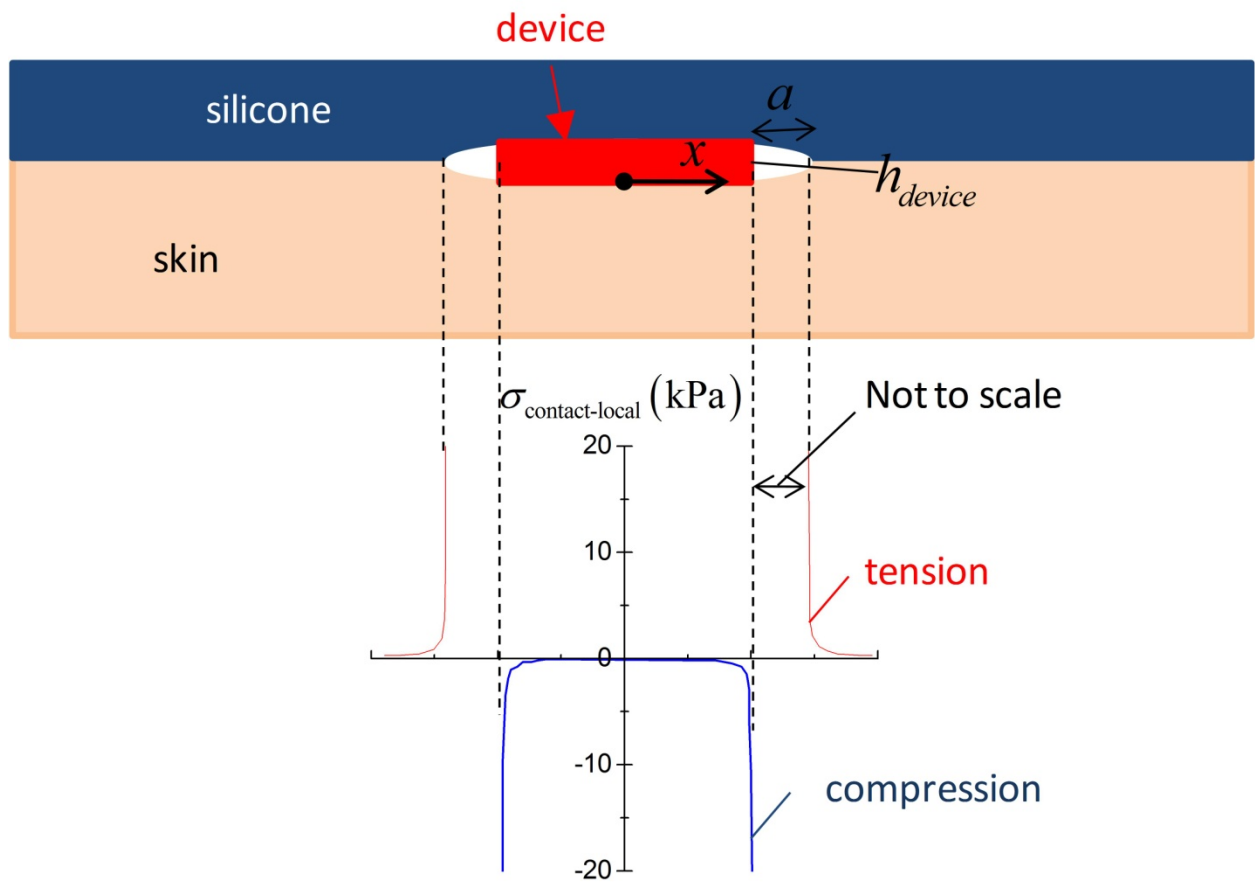


Fig. S11. Schematic cross-sectional view of EES at the interface between skin and silicone (top) and local stress distribution along the FS-EES/skin interface (bottom).

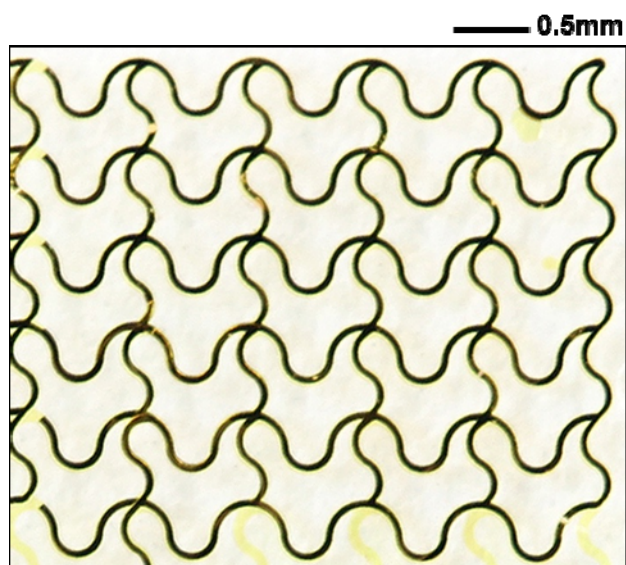


Fig. S12. Image of an FS-EES EP sensor on silicone /PVA substrate.

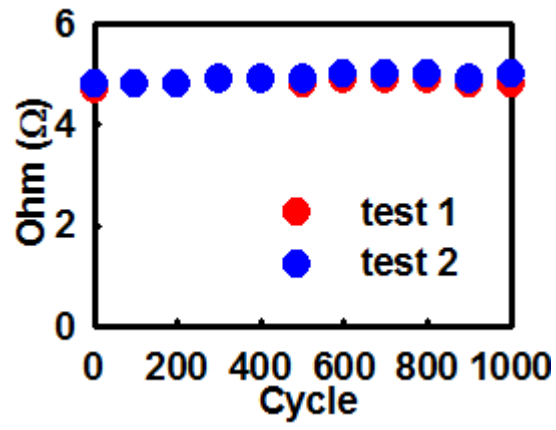


Fig. S13. Fatigue test result for an FS-EES device under repetitive 30% tensile stretching.

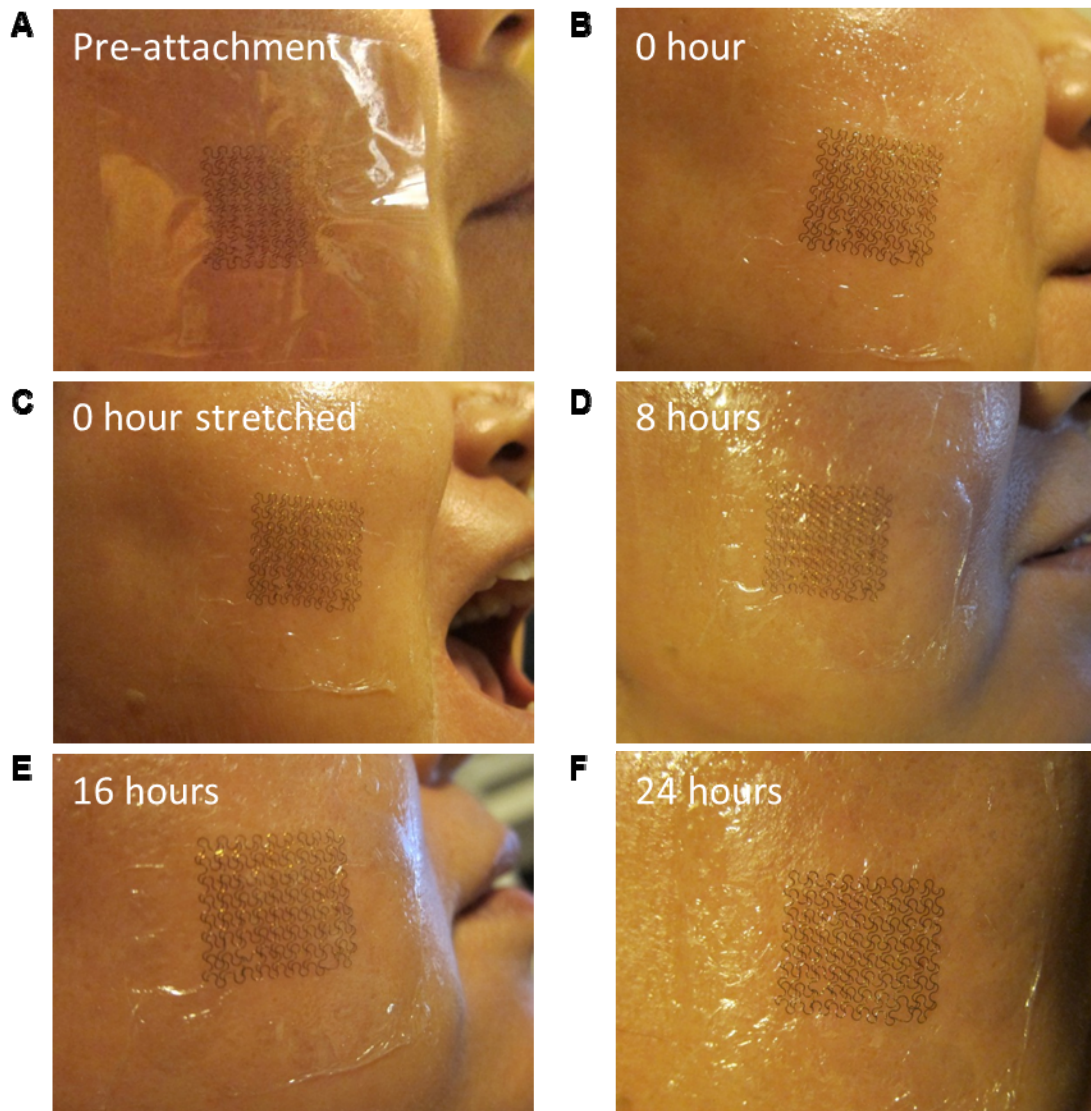


Fig. S14. Results from durability test of an FS-EES mounted on the cheek. **(A)** EES on PVA before attachment. **(B)** Immediately after dissolving away PVA at resting position. **(C)** Immediately after attachment, and under deformation. **(D)** 8 hours after attachment and repeated jaw movements. **(E)** 16 hours after attachment. **(F)** 24 hours after attachment, the device was still intact and no obvious irritation to the skin was observed.

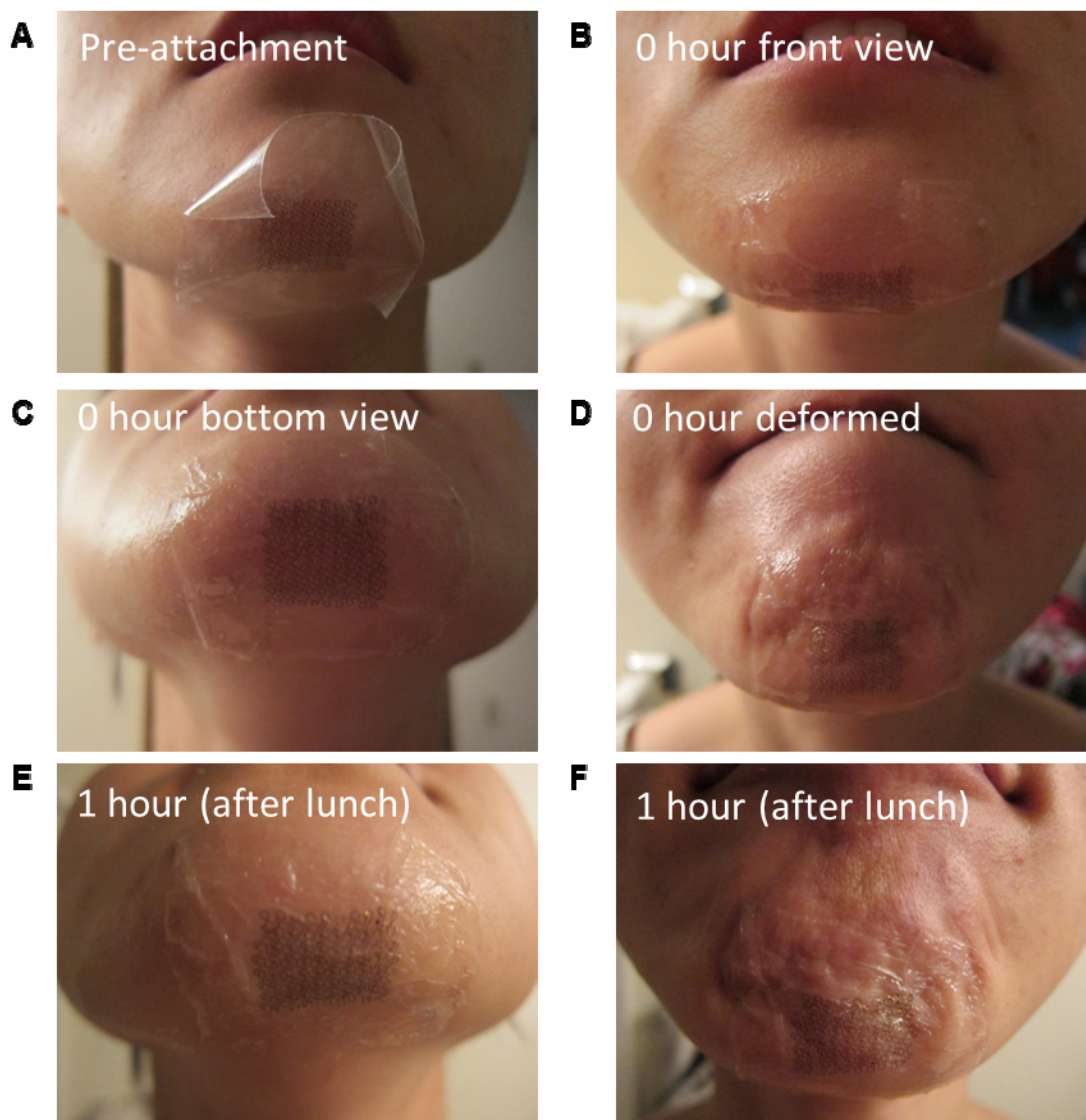


Fig. S15. Results from durability test of an FS-EES mounted on the anterior edge of the chin/jaw. **(A)** EES on PVA before attachment. **(B)** Front view of the device at resting position immediately after dissolving away the PVA. **(C)** Bottom view of the device at resting position immediately after attachment. **(D)** Front view of the devices under deformation immediately after attachment. **(E)** Bottom view of the device at resting position 1 hour after attachment and after lunch, during which repeated chewing and swallowing induced many cycles of loading and deformation of the

device. **(F)** Front view of the devices under deformation 1 hour after attachment and after lunch.

The EES was still intact and no obvious irritation to the skin was observed.

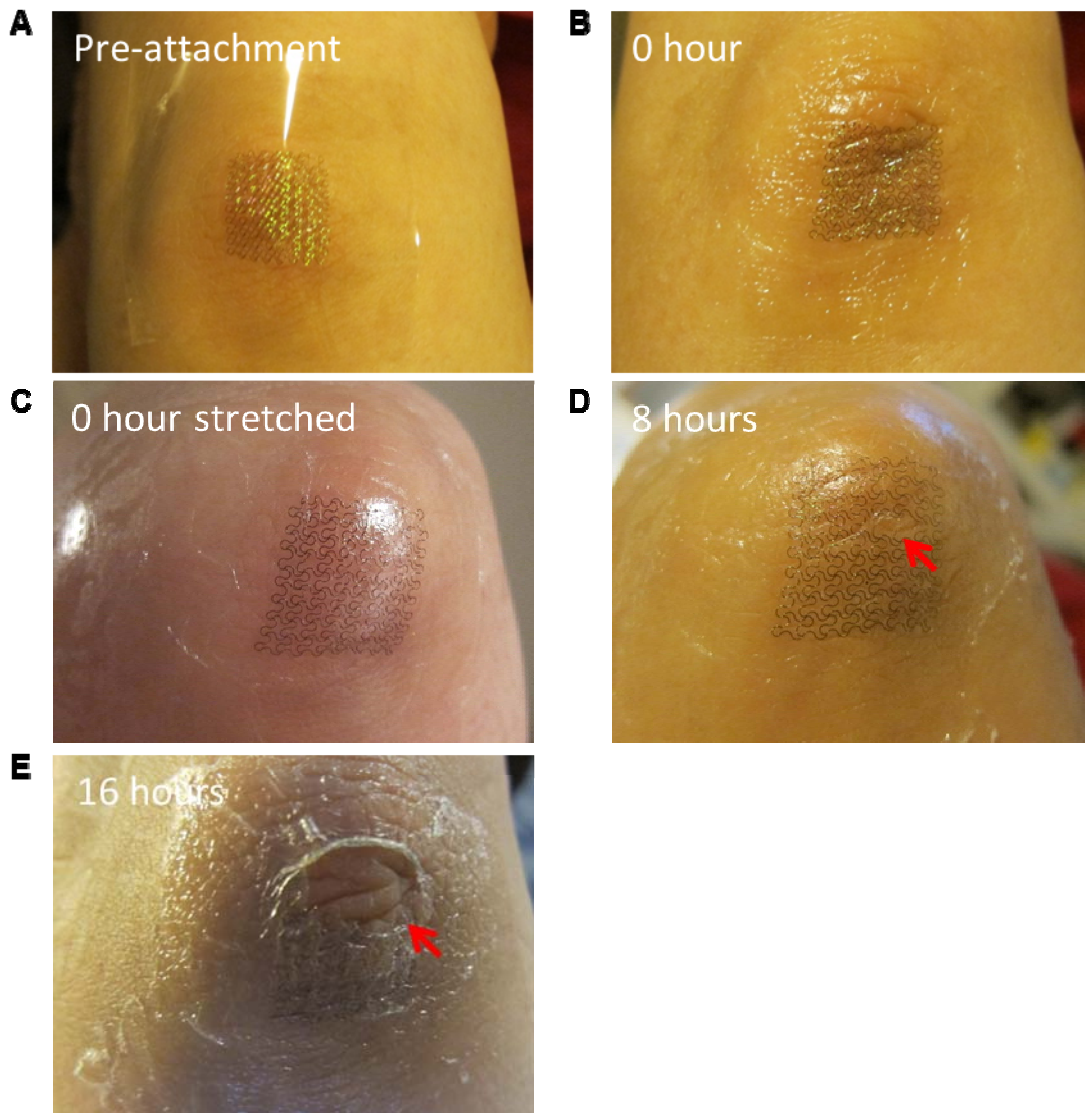


Fig. S16. Results from durability test of an FS-EES mounted on the elbow. **(A)** View of the device on PVA before attachment. **(B)** Immediately after dissolving away PVA at resting position. **(C)** Immediately after attachment, in a stretched position. **(D)** 8 hours after attachment and repeated elbow movements. Here, some degradation of the device EES is apparent, although no skin irritation was observed. **(E)** 16 hours after attachment and cyclic elbow movements, the device was heavily damaged.

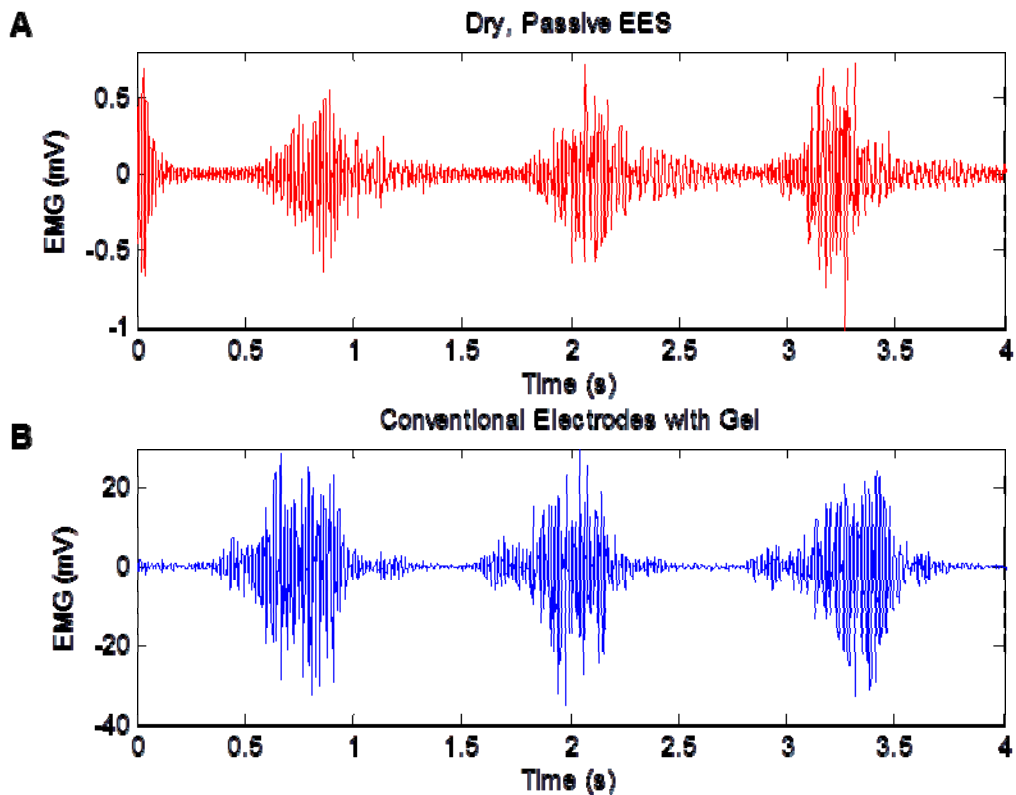


Fig. S17. High-pass filtered EMG signals recorded by (A) passive dry EES and (B) conventional passive electrode with conductive gel. The experimental setups were the same as those used in the SOM Movie S2: the ground electrode was mounted on the right ankle, the reference electrode was mounted near the interior of left elbow, and the recording electrode was placed 8 cm to the anterior of the reference.

Movie S1. A movie clip that illustrates the EES mounting procedure, deformations and extreme flexibility after detachment. The movie also shows an EES mounted on a commercial temporary transfer tattoo.

Movie S2. A movie clip that illustrates real-time EMG waveforms recorded from left forearm. The time horizon on the monitor is 8 s. The movie starts with 1 s of resting and is followed by 8 repetitions of grasping and opening of the left hand over the next 19 s. Each grasping lasts about 2 s and elicits the signature high-frequency oscillations of EMG, which disappears as soon as the hand opens. The measurement was done using dry, passive EES devices for all electrode-skin contacts, without any conductive gel anywhere. The stratum corneum was exfoliated with Scotch tape for recording and reference electrodes. The ground electrode was mounted on the right ankle, the reference electrode was mounted near the interior of left elbow, and the recording electrode was placed 8 cm to the anterior of the reference.